Chaos in Bohmian quantum mechanics

Chaos in Bohmian quantum mechanics

C Efthymiopoulos and G Contopoulos

Research Center for Astronomy, Academy of Athens, Soranou Efesiou 4,
GR-115 27 Athens, Greece

E-mail: cefthim@cc.uoa.gr and gcontop@cc.uoa.gr

Abstract

This paper presents a number of numerical investigations of orbits in the de Broglie–Bohm version of quantum mechanics. We first clarify how the notion of chaos should be implemented in the case of Bohmian orbits. Then, we investigate the Bohmian orbits in three different characteristic quantum systems: (a) superposition of three stationary states in the Hamiltonian of two uncoupled harmonic oscillators with incommensurable frequencies, (b) wave packets in a Hénon–Heiles-type Hamiltonian and (c) a modified two-slit experiment. In these examples, we identify regular or chaotic orbits and also orbits exhibiting a temporarily regular and then chaotic behaviour. Then, we focus on a numerical investigation of the Bohm–Vigier (Bohm and Vigier 1954 *Phys. Rev.* **26** 208) theory, that an arbitrary initial particle distribution P should asymptotically tend to $|\psi|^2$, by considering the role of chaotic mixing in causing irregularity of Madelung's flow, a necessary condition for P to tend to $|\psi|^2$. We find that the degree of chaos of a particular system correlates with the speed of convergence of P to $|\psi|^2$. In the case of wave-packet dynamics, our numerical data show that the time of convergence scales exponentially with the inverse of the effective perturbation from the harmonic oscillator Hamiltonian. The latter result can be viewed as a quantum analogue of Nekhoroshev's (Nekhoroshev 1977 *Russ. Math. Surveys* **32** 1) theorem of exponential stability in classical nonlinear Hamiltonian dynamics.

PACS numbers: 05.45.Mt, 03.65.Ta

1. Introduction

The so-called 'causal' or 'ontological' interpretation of quantum mechanics (de Broglie 1926a, 1926b, 1927a, 1927b, Bohm 1952a, 1952b) is a version of quantum mechanics based on orbits, which gives equivalent results with the usual (Copenhagen) quantum mechanics. Details of this theory are provided in the books of Bohm and Hiley (1993) and Holland (1993).

The de Broglie–Bohm theory was criticized by Pauli (1953), Keller (1953), von Neumann (see Jammer (1974)), Kochen and Specker (1967) and others. Replies to these criticisms were provided by Dewdney and Malik (1993), and in the above books of Bohm and Hiley and Holland. In particular, Holland (1993, pp 24–6) provided detailed answers to the various criticisms of Bohm's theory. Another detailed discussion of criticisms was made by Passon (2005), who also included extensive references.

Some people think that Bohm's theory is a 'hidden variables' theory that can be refuted by the violation of Bell's inequalities (Bell 1965, 1976, 1987), which was verified experimentally by Aspect *et al* (1982). However, Bell's theorem excludes only local hidden variables, while Bohm's theory is nonlocal (see, for example, Dewdney (1992)). In fact, Bell was always an advocate of Bohm's theory.

The main postulates of Bohmian mechanics are

(a) The electron (or any other small particle) has a well-defined position that follows a causally defined trajectory guided by a physically real field, the $\psi(\vec{r}, t)$ field.

(b) The ψ-field satisfies Schrödinger's equation

$$\left(-\frac{1}{2}\nabla^2 + V(\vec{r}, t)\right)\psi = \mathrm{i}\frac{\partial\psi}{\partial t} \tag{1}$$

where we have taken $m = \hbar = 1$.

(c) The particle's orbit is determined by the initial particle's position and by the pilot-wave equation of motion

$$\frac{\mathrm{d}\vec{r}}{\mathrm{d}t} = \mathrm{Im}\left(\frac{\nabla\psi(\vec{r}, t)}{\psi(\vec{r}, t)}\right). \tag{2}$$

This equation implies Newton's equation of motion in a potential

$$U(\vec{r}, t) = V(\vec{r}, t) + Q(\vec{r}, t) \tag{3}$$

where $Q(\vec{r}, t)$ is the 'quantum potential', i.e., an extra term in the potential that guides the particle's motion. The quantum potential is derived by the ψ-field:

$$Q(\vec{r}, t) = -\frac{1}{2}\frac{\nabla^2|\psi|}{|\psi|}. \tag{4}$$

(d) The probability distribution of an ensemble of particles guided by the same ψ-field is $P(\vec{r}, t) = |\psi(\vec{r}, t)|^2$.

Bohmian orbits defined as above are equivalent to the streamlines of a quantum probability flow (Madelung 1926), a fact that allows one to formulate quantum mechanics in terms of the orbits of the fluid elements in a quantum hydrodynamical model (Skodje *et al* 1989, Holland 2005). Thus, the dynamical behaviour of these orbits is of interest both in the conventional and in the Bohmian versions of quantum mechanics.

The nonlocality of the Bohmian mechanics proceeds from the fact that the particle orbits depend on the ψ-field which is given as a solution of the Schrödinger equation independently of the positions and the motions of the particles. In particular, the $\psi-$ field is not generated by particles as in the case of electromagnetism.

While postulates (a)–(c) lead to the same results as in the usual quantum mechanics, postulate (d) has received particular criticism (Pauli 1953, Keller 1953), based on the following remarks. If the initial distribution $P(x, 0)$ is selected as $P(x, 0) = |\psi(x, 0)|^2$, the equation $P(x, t) = |\psi(x, t)|^2$ is fulfilled at any later time t. This follows trivially from the properties of the Madelung flow. However, as emphasized by Bohm and Hiley (1993), the particles' distribution is *not* the source of the ψ-field. Therefore, while in quantum fluid dynamics the initial distribution of the fluid elements is by definition equal to $|\psi(x, 0)|^2$, in Bohmian

mechanics the initial particle distribution $P(x, 0)$ can be an arbitrary distribution, different in general from $|\psi(x, 0)|^2$. In that case, it may be that $P(x, t)$ and $|\psi(x, t)|^2$ do not become identical at some later time t.

In order to address this point, Bohm (1953) considered random collisions of the particles, that form the initial distribution $P(x, 0)$, with other particles or external fields. These collisions change $P(x, t)$ in such a way that it will converge to $|\psi(x, t)|^2$. However, such an approach introduces an effect which is outside the ensemble of the particles themselves. On the other hand, Bohm and Vigier (1954) have developed a statistical mechanics of particles following Bohmian orbits. They assert that, independently of the choice of $P(x, 0)$, $P(x, t)$ will tend asymptotically to $|\psi(x, t)|^2$ as $t \to \infty$, on the assumption that the Madelung's flow satisfies a *mixing* property, namely that "a fluid element starting in an elementary element of volume dx', in a region where the fluid density is appreciable, has a nonzero probability of reaching any other element of volume dx in this region" (Bohm and Vigier 1954).

One way to justify this assumption is by considering the statistical properties of systems with a large number of interacting degrees of freedom. Valentini (1991) has put forward a relevant argument, assuming that systems composed by a large number of interacting degrees of freedom have the mixing property. Another approach to the same problem was undertaken by Dürr, Goldstein and Zanghi (1992a, 1992b). These authors have argued that the $|\psi|^2$ distribution in Bohmian mechanics is an 'equilibrium' distribution, similar to the thermodynamical equilibrium in statistical mechanics, that arises naturally in a 'Bohmian universe' for typical configurations of the 'universe'.

These approaches notwithstanding, the theory of Bohm and Vigier, in its original formulation, does not depend on the number of degrees of freedom of a quantum system. Thus, it is of interest to study the extent of its applicability also in systems with a small number of degrees of freedom. In section 3 of Bohm and Vigier (1954) arguments are given that the mixing behaviour of the probability fluid, which is described by Bohmian orbits, is a generic property in quantum mechanical systems that should be expected as a result of the very *irregular character of Madelung's flow*. In the authors' words, "it is clear that if we followed a given fluid element, we would discover that it undergoes an exceedingly irregular motion, which is able in time to carry it from any specific trajectory of the mean Madelung motion to practically any other trajectory". This description was refined by Bohm and Hiley (1993), by stressing the fact that in most quantum systems the quantum potential undergoes such rapid fluctuations, in space and time, that Bohmian orbits should be expected to show *chaotic* behaviour.

The meaning of chaos in quantum mechanics is still an open question. This is reflected in the variety of definitions of quantum chaos, or quantum integrability, that exist in the literature. Well-known examples are

(a) In the book of Gutzwiller (1990), quantum chaos is determined in terms of the difference in the quantum behaviour between systems which are classically integrable or classically chaotic. Such differences are manifested in a number of quantum properties such as the degree of repulsion of the energy levels (quantified by a Poisson or Wigner distribution), the irregularity of nodal patterns for particular quantum states, or the different dynamical behaviour of Wigner-type distributions of wave packets, which are quantum analogues of the classical Liouville phase-space density.

(b) A definition of quantum integrability based on the existence of a sufficient number of globally defined, non-singular operators with vanishing commutators (see Robnik (1986) for a review) corresponds to the fact that a system which is quantum integrable in the above sense shows localization of the eigenfunctions on a set of invariant tori of the corresponding classical system that can be approximated by a semiclassical quantization procedure (see also

Berry (1979)). However, as emphasized by Robnik (1986), localization of the eigenfunctions is also manifested in classically chaotic systems (e.g., the stadium billiard), therefore it is not a property of only integrable systems.

(c) There is a theorem by Kosloff and Rice (1981) which claims that bounded quantum mechanical systems cannot have chaotic motion. As shown by Manz (1989), this claim can be based on the linearity of the Schrödinger equation itself.

The above definitions notwithstanding, Bohmian mechanics defines quantum chaos as a genuine quantum property, i.e., a property of the orbits evolving under the action of the quantum potential, which is irrespective of the behaviour of orbits in the corresponding classical potential. In particular, systems which are classically integrable, or very close to integrable, may exhibit a large degree of chaos in the Bohmian sense, because of fluctuations of the quantum potential Q. The opposite is also possible as we will see in section 3. Namely, classically chaotic systems may not be chaotic quantum-mechanically.

Quantum chaos in the framework of Bohm's theory was considered by Dürr *et al* (1992a). Further work on this problem was done by Schwengelbeck and Faisal (1995) and Parmenter and Valentine (1995). These two papers defined quantum chaos of Bohmian orbits in terms of the Lyapunov characteristic number (LCN, see section 2), or the Kolmogorov entropy, which is equal to the sum of positive Lyapunov numbers. The first application of this method was on the quantum kicked rotor, i.e., the quantum standard map (Schwengelbeck and Faisal 1995). They found that this system has zero LCN, thus it should not be chaotic. The same result was found by Dewdney and Malik (1996), who, however, found chaos in the Bohmian orbits of the kicked rotor system when the latter is repeatedly interacting with a measuring apparatus. On the other hand, Faisal and Schwengelbeck (1995) found that a quantum generalization of Arnold's cat map has positive LCN, thus it is chaotic. An explanation of this difference of behaviour between these two maps will be provided in section 3.

Parmenter and Valentine (1995) found quantum chaos in a very simple classically integrable system (uncoupled oscillators). They found chaos if (a) the system has at least two degrees of freedom and (b) the ψ-field is a solution of Schrödinger's equation defined as the superposition of at least three stationary states, where at least one pair of these states have incommensurable eigenvalues. But they also claimed that all aperiodic orbits in a ψ-field with the above conditions are chaotic. However, as shown in the present paper (section 3), their conclusion is an artefact of a wrong method used to measure chaos, while a correct calculation of the LCN indicates that there are both regular or chaotic aperiodic orbits in this quantum system.

On the other hand, Wu and Sprung (1999) provided numerical evidence that all orbits in ψ-fields consisting of the superposition of stationary states with commensurable eigenvalues, as for example in 2D billiards with commensurable lengths of the billard's sides, are periodic, thus they exhibit no chaos. Makowski *et al* (2000) found chaos in some cases represented by only two stationary states in a system of two degrees of freedom, while Parmenter and Valentine (1997) found that we may have chaos in the case of even one stationary state, if the number of degrees of freedom is at least 4.

Ordered (quasi-periodic) and chaotic orbits in quantum systems corresponding to classically integrable systems were also found by de Sales and Florencio (2003). These authors calculated the forms of the orbits, the power spectrum and the Lyapunov characteristic numbers. They also calculated two surfaces of section, but rather incompletely (only for two orbits in each case). A more complete treatment was given by Iacomelli and Pettini (1996), who not only found chaotic motion, but also calculated a kind of threshold between order and chaos in a particular case (a hydrogen atom interacting with an oscillating electric field) as a function of a nonlinearity parameter. These authors stress the fact that (Bohmian) quantum

chaos exists even at the integrable limit of the classical system; however, quantum chaos increases considerably at the threshold where the classical system becomes largely chaotic. Thus, in that case classical chaos also seems to enhance quantum chaos. The threshold between order and chaos was also considered by Sengupta and Chattaraj (1996) in a Hénon–Heiles Hamiltonian.

A quite different case is that of Bohmian orbits in ψ-fields produced by the time evolution (by Schrödinger equation) of initially minimum uncertainty coherent states. Wisniacki *et al* (2003) calculated sets of Bohmian orbits in such a model and found their probability distribution P that is to be compared with the probability distribution $|\psi|^2$ derived by the ψ-field. These authors conclude that there is a general tendency to agreement between P and $|\psi|^2$, although the details of the two distributions are not the same (e.g., the survival probability function, determined by the Wigner function, shows some maxima in the case of the Bohmian distribution P that are not present in the distribution $|\psi|^2$). Further work on wave packets was done by de Polavieja (1996), who found that there are both regular and chaotic orbits in a wave packet evolving in a Yang–Mills-type potential, and by Falsaperla and Fonte (2003), who considered orbits near the nodal lines of a time-independent wave packet. In particular, de Polavieja (1996) found Bohmian orbits which are ordered for some intervals of time and chaotic during other intervals of time. As we will see in section 3, the numerical evidence is that, after some initial transient interval of time, the LCN tends to stabilize to a limiting value for a time of integration long enough, so that an orbit can be definitely characterized as ordered or chaotic.

A final case is that of the two-slit experiment. While the maxima of the density of Bohmian orbits in this experiment reproduce an interference pattern (Philippidis *et al* 1979), these orbits do not cross. Therefore, they do not fulfil the mixing hypothesis of the Bohm–Vigier theory. Oriols *et al* (1996) also emphasize the consequences of non-crossing Bohmian orbits. However, Holland and Philippidis (2003) found that a spin-dependent term changes the results so that two orbits may cross each other and the axis of symmetry. Another difficulty, as regards the definition of chaos in two-slit experiments, is that the phase space is not compact (see section 2).

The purposes of the present paper are the following:

(1) We seek to clarify the meaning and the degree of chaos in Bohmian mechanics. This subject is not yet completely clarified. As Holland (1993) remarks, "classifying the quantum paths, . . . , and defining analogues of Kolmogrov entropy is a largely uncharted territory". To this end, we first explain how the classical notion of chaos should be implemented in the case of Bohmian orbits. Then we study the orbits in 2D systems, some of which are or are not classically integrable. In particular, we consider three basic cases: (a) a superposition of three stationary states in 2D uncoupled harmonic oscillators with incommensurable frequencies, (b) a coherent wave packet in the Hénon–Heiles and in the integrable Hénon–Heiles 2D Hamiltonian and (c) a modified two-slit experiment. In these systems, we identify regular and chaotic orbits, as well as orbits that exhibit a temporarily regular and then chaotic behaviour.

(2) We numerically examine the extent of validity of the Bohm–Vigier theory, in connection with the regular or chaotic character of ensembles of orbits guided by a particular ψ-field. One particular example, where the particle distribution P tends to the $|\psi|^2$ distribution in a square box potential, was given by Valentini and Westman (2005). In the present paper, we identify cases when (a) P and $|\psi|^2$ tend to coincide asymptotically in time or (b) do not coincide at any time. In the case where P tends to $|\psi|^2$ asymptotically, the time of relaxation correlates with the Lyapunov time of orbits. A similar result was found by Bowman (2002) in a kicked rotator model.

(3) We also find that in $\psi-$ fields formed by initially coherent states, the convergence between P and ψ^2 starts taking place as soon as the packet starts losing its coherence. In the case of two harmonic oscillators coupled with a nonlinear perturbation, the numerical evidence is that this happens at times exponentially long in the inverse of the effective perturbation. This result is a quantum analogue of Nekhoroshev's (1977) exponential stability of orbits in classical Hamiltonian dynamics. On the other hand, in the case of uncoupled harmonic oscillators the packets are known to remain coherent for all times.

The paper is organized as follows: section 2 gives a definition of chaotic orbits in terms of the Lyapunov characteristic number. We stress the necessary conditions for the appearance of chaos in systems with time-dependent potentials (classical or quantum). Section 3 presents the calculation of ordered and chaotic orbits in the quantum systems mentioned in (1) above. In section 4, we numerically check whether the probability P tends to $|\psi|^2$ as required by the Bohm–Vigier theory in the same systems. We also provide evidence that the approach of P to $|\psi|^2$ occurs at exponentially long times, as in the Nekhoroshev theorem. Finally, we find a correlation between the degree of applicability of the Bohm–Vigier theory and the regular or chaotic character of the associated Bohmian orbits. Section 5 summarizes the main conclusions of the present study.

2. Chaos in time-dependent potentials

The usual notion of chaos (see Contopoulos (2004) for a review) refers to orbits that satisfy the following two conditions:
(a) they are embedded in a compact phase space;
(b) they show extreme sensitivity to the initial conditions.

Property (b) is usually quantified by the Lyapunov characteristic number (LCN), which measures the growth rate of deviations between nearby orbits. In the case of chaotic orbits, deviations grow exponentially in time, while in the case of regular orbits they grow algebraically (usually linearly) in time. However, property (b) alone is not sufficient for the characterization of an orbit as chaotic; property (a) is also necessary. The importance of the compactness condition (implying that the phase-space volume that is accessible to the orbit is finite) can be demonstrated by the following elementary example. Consider the one degree of freedom Hamiltonian:

$$H = \tfrac{1}{2}\big(p_x^2 - x^2\big). \tag{5}$$

Except for a residual set of orbits approaching asymptotically the origin, all other orbits in this Hamiltonian, and their deviations, grow exponentially in time, i.e., asymptotically as e^t. Thus, the Lyapunov characteristic number is positive (LCN $= 1$). However, the system is integrable and exhibits no chaos. But the phase space of this system is not compact, as the level curves of constant energy are hyperbolas, or straight lines. Therefore, one cannot speak about chaos in such a system, even though the LCN can be defined for all orbits and it is generically positive.

A second example refers to the orbit of a distant star that crosses a gravitationally bound stellar system, e.g., a galaxy. As long as the star is far from the galaxy, the star 'feels' the galaxy almost as a point mass, i.e., the force on the star is effectively Keplerian. When the star comes close to the galaxy, it may be chaotically scattered by it. However, after the scattering the star goes away from the galaxy and the force becomes again Keplerian. Thus, the LCN tends asymptotically to zero, while the orbit has definitely undergone an interval of chaotic motion. In that case too we cannot speak about chaos as the phase space is not compact, but we can only speak about chaotic scattering of the orbit.

Assuming that condition (a) is fulfilled, the Lyapunov characteristic number is calculated as follows (Benettin *et al* 1976). Given a set of evolution equations

$$\frac{d\mathbf{x}}{dt} = \mathbf{f}(\mathbf{x}, t) \tag{6}$$

(where $\mathbf{x}$ is n dimensional), one determines the set of variational equations

$$\frac{d\delta\mathbf{x}}{dt} = \nabla_{\mathbf{x}}\mathbf{f}(\mathbf{x}, t)\delta\mathbf{x} \tag{7}$$

that are to be solved together with the original equations. One then calculates the limit

$$\text{LCN} = \lim_{t \to \infty} \frac{1}{t} \ln \frac{\xi(t)}{\xi(0)} \tag{8}$$

where $\xi(t)$ is the norm of the deviation vector

$$\xi(t) = \sqrt{\delta x_1^2(t) + \cdots + \delta x_n^2(t)}. \tag{9}$$

(Other metrics in the definition of $\xi(t)$ give the same LCN in general.) If $\alpha = \text{LCN} > 0$, the deviations grow on the average exponentially, as $\xi(t) = \xi(0) e^{\alpha t}$, and the orbit is called chaotic. On the other hand, if $\text{LCN} = 0$, the deviations can grow at most as a power law (usually, they grow linearly in time, i.e., $\xi(t) = \xi(0) + At$ with $A = \text{const}$).

Numerically, one cannot calculate exactly the limit (8), but only a finite-time Lyapunov number

$$\chi(t) = \frac{1}{t} \ln \frac{\xi(t)}{\xi(0)} \tag{10}$$

for a time t much larger than the characteristic dynamical time of the system. There is therefore only an indication that an orbit is regular or chaotic. Namely, along regular orbits $\chi(t)$ behaves as the asymptotic limit of $\ln t/t$, i.e. $\chi(t) \propto 1/t$, while along chaotic orbits the quantity $\chi(t)$ tends to stabilize at a final value.

In Hamiltonian systems with time-dependent potentials

$$H(q, p, t) = \frac{p^2}{2} + V(q, t) \tag{11}$$

one may consider an extended phase space in which time is one more canonical variable, with energy being its canonical momentum. The question is whether these variables should be taken into account in the variational equations. The answer is that the results with or without taking them into account are equivalent. This is because energy deviations can grow only linearly, so that the length of the deviation vector in the extended phase space, say $\xi'(t)$, is given by $\xi'(t) = \xi(t) + Bt = e^{\alpha t} + Bt$. Thus, $\xi'(t)$ gives the same LCN as $\xi(t)$. An example of this type of calculation is given in figure 1, referring to the Duffing-type Hamiltonian

$$H(x, p, t) = \frac{p^2}{2} - \frac{x^2}{2} + \frac{\epsilon}{4}x^4 - Bx \cos(\omega t) \tag{12}$$

where $\omega = (\sqrt{5} - 1)/2$, $\epsilon = 0.25$, $B = 0.1$. Figure 1(a) shows four orbits in a stroboscopic Poincaré surface of section $(x(mT), p(mT))$, with $m = 1, 2, \ldots$ and $T = 2\pi/\omega$. Figure 1(b) shows a calculation of the LCN by the $\chi(t)$ method for these orbits. Thus, we find that $\chi(t)$ falls asymptotically as $1/t$ for the regular orbits A, C, D which define invariant curves on the Poincaré surface of section (figure 1(a)). On the other hand, $\chi(t)$ tends to stabilize at a positive value for the chaotic orbit B.

Some people claim to calculate the Lyapunov characteristic number by considering the sum of the greatest real parts of the eigenvalues of the Jacobian matrix corresponding to the
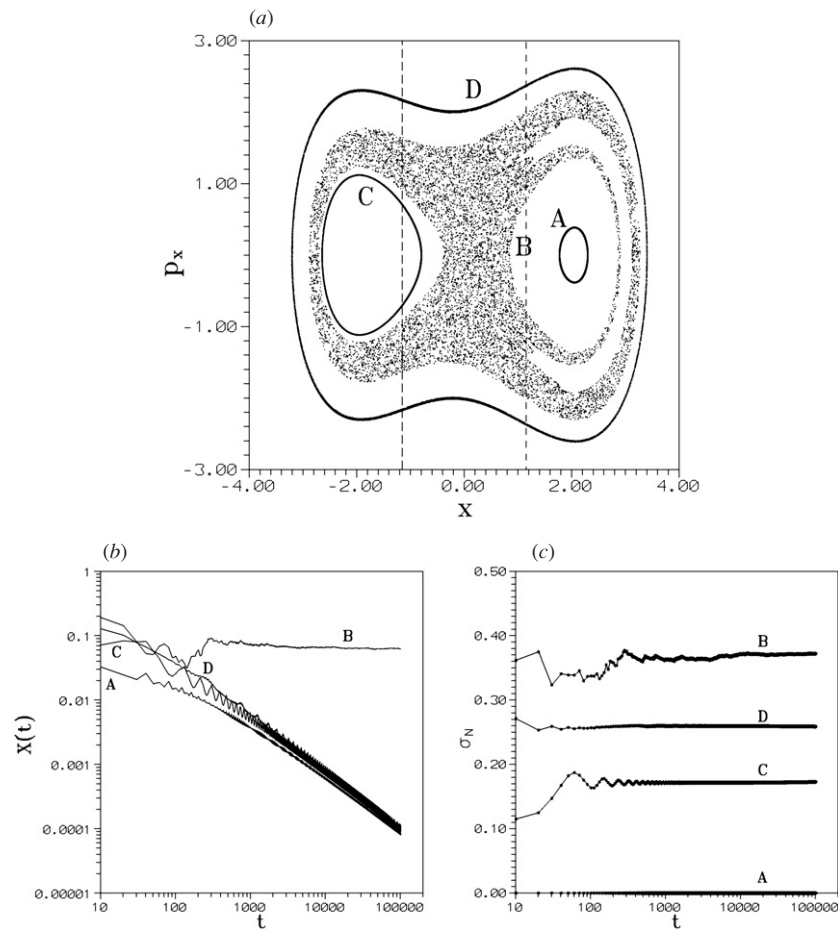
Figure 1. (*a*) Stroboscopic Poincaré surface of section for orbits in the Hamiltonian (12). The initial conditions of the orbits are (A) $x = 2.3$, $p_x = \dot{x} = 0$, (B) $x = 0.3$, $p_x = 0$, (C) $x = -1$, $p_x = 0$, (D) $x = 0$, $p_x = 2$. (*b*) The time evolution of the function $\chi(t)$ (equation (10)) for the same orbits. (*c*) The time evolution of the quantity σ_N (equation (13)) for the same orbits.

variational equations of motion. For example, Parmenter and Valentine (1995) define the quantity

$$\sigma_N = \frac{1}{N} \sum_{n=1}^{N} (\text{Re } \lambda_n)_{\max} \tag{13}$$

where $(\text{Re } \lambda_n)_{\max}$ is the greatest real part of the eigenvalues of the Jacobian matrix J_n of the variational equations at the *n*th integration step. It is then claimed that LCN $= \lim_{N \to \infty} \sigma_N$. However, this claim is not correct as the variational vector $\delta\mathbf{x}$ is not parallel to the direction of the eigenvector with the largest positive eigenvalue, but it is always tangent to an invariant curve, for regular orbits, or an asymptotic curve for chaotic orbits (Voglis *et al* 1998). For example, the Jacobian matrix of the variational equations for the Hamiltonian (12)

$$J(t) = \begin{pmatrix} 0 & 1 \\ 1 - 3\epsilon x(t)^2 & 0 \end{pmatrix} \tag{14}$$

yields the eigenvalues $\lambda = \pm\sqrt{1 - 3\epsilon x(t)^2}$, which are real in the interval $\left(-\frac{1}{\sqrt{3\epsilon}} \leqslant x(t) \leqslant \frac{1}{\sqrt{3\epsilon}}\right)$ (in the zone between the dashed lines of figure 1(a)). If an invariant curve happens to partially belong to this zone, the quantity σ_N is positive for an orbit on this curve, thus it cannot be equal to the LCN which is zero. For example, figure 1(c) shows the quantity σ_N for the four orbits A, B, C, D. The result with σ_N is correct for the orbits A (regular, outside the zone) and B (chaotic). However, σ_N turns out to be positive for the regular orbits C, D which cross the zone, although these orbits are ordered. Therefore, the quantity σ_N is not a good criterion for chaos.

3. Ordered and chaotic orbits in Bohmian mechanics

Having determined the method that we use for the characterization of orbits, we proceed now in examining the Bohmian orbits in a number of characteristic examples of quantum systems.

3.1. Uncoupled oscillators with incommensurable frequencies

Our first example refers to Bohmian orbits in the Hamiltonian:

$$H = \tfrac{1}{2}\left(p_x^2 + p_y^2\right) + \tfrac{1}{2}k(x^2 + (\omega y)^2) \tag{15}$$

that was used by Parmenter and Valentine (1995) to define deterministic chaos in Bohmian mechanics. Setting $k = 1, \omega = \sqrt{2}/2$, the spectrum of eigenvalues is given by

$$E_{n,m} = \left(\tfrac{1}{2} + n\right) + \left(\tfrac{1}{2} + m\right)\tfrac{\sqrt{2}}{2} \tag{16}$$

where both n and m are natural numbers $0, 1, 2, \ldots$. The corresponding eigenfunctions are

$$\psi_{n,m}(x, y, t) = \mathrm{e}^{-\mathrm{i}E_{n,m}t} \exp\left(-\frac{x^2 + y^2/2}{2}\right) H_n(x) H_m(\sqrt{2}y/2) \tag{17}$$

where $H_n(x)$ is the nth Hermite polynomial. Parmenter and Valentine study Bohmian orbits in the ψ-field created by the superposition of three such stationary states:

$$\psi(x, y, t) = \psi_{0,0}(x, y, t) + a\psi_{1,0}(x, y, t) + b\psi_{1,1}(x, y, t). \tag{18}$$

The corresponding quantum potential (equation (4)) is time dependent. In fact, for any choice of eigenvalues with $n, m \neq 0$, the time dependence of the quantum potential is through trigonometric functions $\mathrm{e}^{\mathrm{i}(\mu+\lambda\omega)t}$, with μ, λ being the integers. Since ω is an irrational number, there is no period $t = T$ that is the same for all trigonometric terms. Therefore, this can be called an 'aperiodic' potential.

Figures 2 and 3 refer to the calculation of the Lyapunov characteristic number for Bohmian orbits in the ψ-field (18). Figures 2(a) and 3(a) show the same orbits as figures 1 and 3 of Parmenter and Valentine (1995), calculated for a longer time ($t \leqslant 1000$ and $t \leqslant 300$, respectively). The irregular pattern of the orbit of figure 2(a) indicates that this orbit is chaotic. On the other hand, the orbit of figure 3(a) looks very regular. In fact, this orbit is reminiscent of classical 'box' orbits in perturbed harmonic oscillators with incommensurable frequencies, i.e., the orbit fills a deformed parallelogram (see, for example, Contopoulos (2004)). However, classical box orbits have reflections only on the edges of the deformed parallelogram, while the orbit of figure 3(a) has many reflections of $y(t)$ that take place in the interior of the parallelogram. Therefore, this orbit should be distinguished from a classical box orbit.

Now, based on a computation of the Lyapunov characteristic number, Parmenter and Valentine claim that both these orbits are chaotic, with $\sigma_N \simeq 1.1$ (equation (13)) for the first
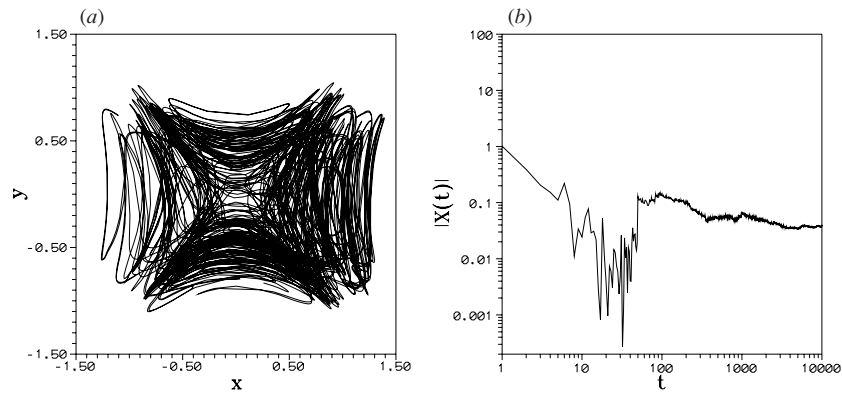
Figure 2. (a) A Bohmian orbit with initial conditions $x_0 = y_0 = 0.1$ in the ψ-field (18), with $a = 1, b = 8$, which is a solution of Schrödinger's equation in the Hamiltonian (15) with $c = \sqrt{2}/2$. The orbit is plotted for a time $0 \leqslant t \leqslant 1000$. (b) The time evolution of the quantity $\chi(t)$ for the same orbit and a longer time ($t \leqslant 10000$). The initial conditions for the variational equations are $\delta x = 1, \delta y = 0$.
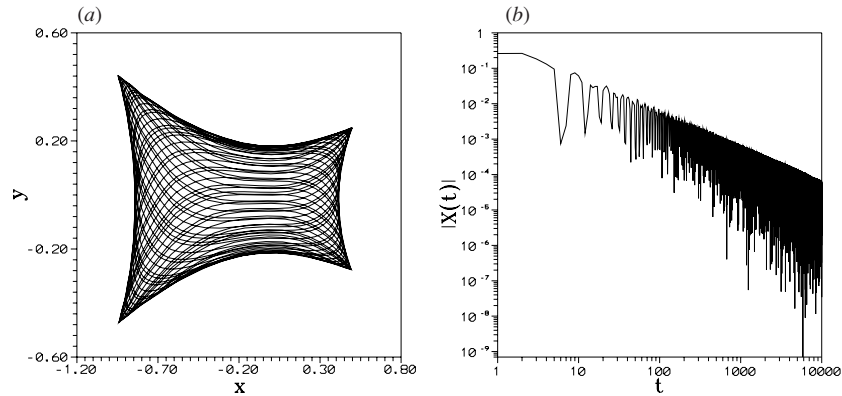

Figure 3. Same as in figure 2, for initial conditions $x_0 = 0.5$, $y_0 = 0.25$, $\delta x = 1, \delta y = 0$ and $a = b = 1, c = \sqrt{2}/2$. The orbit in (a) is plotted for $t \leqslant 300$.

orbit and $\sigma_N \simeq 0.3752$ for the second orbit. However, their calculation is based on adding the eigenvalues of the local Jacobian matrices of the variational equations, and, as demonstrated in section 2, this method does not give the correct LCN. If, instead, one follows the correct definition of the LCN (equations (8) and (9)) based on integration of the variational equations, one finds that the orbit of figure 2(a) is chaotic, while the orbit of figure 3(a) is regular. Figure 2(b) shows the calculation of the LCN for the orbit of figure 2(a) with a numerical solution of the variational equations. The quantity $|\chi(t)|$ initially makes large oscillations. In fact, without the absolute value, $\chi(t)$ oscillates between positive and negative values, so that each crossing of the axis $\chi(t) = 0$ corresponds to a sudden dropping of $|\chi(t)|$ (on a logarithmic scale) to very small positive values. Such droppings are seen in figure 2(b) for times smaller than $t = 100$. However, for times larger than $t = 100$, the quantity $\chi(t)$ stabilizes at a positive value. This limiting value corresponds to LCN $\simeq 0.1$, which is quite different from the value 1.1 found by Parmenter and Valentine, by use of the quantities σ_N instead of the correct LCN (equations (8) and (9)), but this quantitative difference does not

change the qualitative conclusion that the orbit is chaotic. However, this is not so in the case of the orbit of figure 3(*a*). In figure 3(*b*), we plot the logarithm of the absolute value $\ln|\chi(t)|$ in order to see the asymptotic behaviour of the magnitude of $\chi(t)$ on a logarithmic scale. Clearly, the magnitude of $\chi(t)$ decreases as t increases, and the decrease asymptotically follows the power-law $\chi(t) \sim 1/t$. This means that the orbit is ordered and $LCN = \lim_{t\to\infty} \chi(t) = 0$. On the other hand, by repeating the calculation of Parmenter and Valentine, based on the quantity σ_N, we also found a positive value ($\sigma_N \simeq 0.3$). This would erroneously lead to the characterization of the orbit as chaotic, while in fact this orbit is ordered.

In classical mechanics, regular box orbits preserve an additional integral of motion besides the energy. This is usually called a 'third integral' (Contopoulos 1960) and it is a series in the canonical variables. Third integrals in classical time-dependent systems were calculated by Contopoulos (1966). In the present case, this series contains time-dependent trigonometric terms depending on two incommensurable frequencies. A detailed calculation of this series will be presented in a future paper.

Another important point that should be stressed here regards the difference between classical and (Bohmian) quantum chaos. The classical equations of motion are second-order ordinary differential equations. Thus, in order for chaos to appear, a system must be at least (a) two dimensional with time-independent potential $V(x, y)$ or (b) one dimensional with a time-dependent potential $V(x, t)$. On the other hand, the pilot equations (2) are first-order ordinary differential equations. Thus, if a system is one dimensional, it cannot exhibit Bohmian chaos independently of whether its classical potential is time dependent or not. In fact, in a one-dimensional system, the solution of Schrödinger's equation (1) is always a function $\psi(x, t)$ that depends both on x and t, independently of whether the potential V explicitly depends on time or not. It follows that the Bohmian equation of motion (2) is of the form

$$\frac{\mathrm{d}x}{\mathrm{d}t} = f(x, t) \tag{19}$$

with some function $f(x, t)$. Thus, solutions to this equation cannot exhibit chaos.

This simple remark explains why Schwengelbeck and Faisal (1995) find no chaos in the Bohmian orbits of the kicked rotor Hamiltonian, which is the quantum analogue of the strongly chaotic classical standard map, while they find chaos (Faisal and Schwengelbeck 1995) in the quantum cat map. Namely, classically both the standard map and the cat map are paradigms of chaotic two-dimensional systems. On the other hand, quantum mechanically, in the case of the standard map the ψ-field is a solution of the time-dependent Schrödinger equation for the kicked rotor Hamiltonian

$$\left(-\frac{1}{2}\frac{\partial^2}{\partial\theta^2} + k\cos\theta \sum_{N=-\infty}^{\infty} \delta(t - NT)\right)\psi = \mathrm{i}\frac{\partial\psi}{\partial t} \tag{20}$$

with $k = $ const, which yields a one dimensional and time-dependent wavefunction ($\psi(\theta, t)$). Thus, the equation of motion, derived from equation (2), is a first-order, one-dimensional and non-autonomous equation of the form

$$\frac{\mathrm{d}\theta}{\mathrm{d}t} = f(\theta, t)$$

which cannot exhibit chaos. On the other hand, in the case of the quantum Arnold cat map, the ψ-field is a solution of the time-dependent Schrödinger equation

$$\left(-\frac{1}{2}\nabla^2 - \frac{\mathrm{i}}{2}(\nabla \cdot \mathbf{V} \cdot \mathbf{x} + \mathbf{x} \cdot \mathbf{V} \cdot \nabla) \sum_{N=-\infty}^{\infty} \delta(t - NT)\right)\psi = \mathrm{i}\frac{\partial\psi}{\partial t} \tag{21}$$
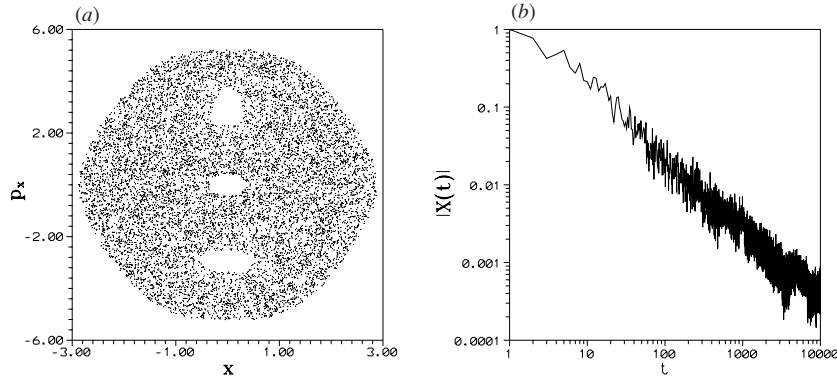
Figure 4. (*a*) Poincaré section for an orbit with initial conditions $x_0 = p_{x0} = 1$ in the Hamiltonian (22) with $\omega = (\sqrt{5}-1)/2$, $\epsilon = 3$ and $2\sigma^2 = 5$. (*b*) The evolution of $\chi(t)$ for a Bohmian orbit with the same initial conditions guided by a ψ-field which is initially a minimum uncertainty coherent state centred at (x_0, p_{x0}).

where $\mathbf{x} \equiv (x_1, x_2)$, $\nabla = \left(\frac{\partial}{\partial x_1}, \frac{\partial}{\partial x_2}\right)$ and $\mathbf{V}$ is a 2×2 matrix defined by $e^{\mathbf{V}} = \mathbf{C}$, with $C_{11} = C_{12} = C_{21} = 1$ and $C_{22} = 2$. Thus, the solution of equation (21) is a two dimensional and time-dependent function $\psi(x_1, x_2, t)$, which yields, through equation (2), a system of two first-order, non-autonomous, equations of motion of the form

$$\frac{\mathrm{d}x_1}{\mathrm{d}t} = f_1(x_1, x_2, t)$$

$$\frac{\mathrm{d}x_2}{\mathrm{d}t} = f_2(x_1, x_2, t).$$

Such a system may in principle yield chaos, as indeed found by these authors.

In order to numerically demonstrate the above remark, figure 4(*a*) shows the classical Poincaré surface of section of the Hamiltonian

$$H = \frac{1}{2}(p^2 + x^2) + \frac{\epsilon}{4}x^4 \exp(-x^2/2\sigma^2) \cos(\omega t) \tag{22}$$

for $\omega = (\sqrt{5}-1)/2$, $\epsilon = 3$ and $2\sigma^2 = 5$, in which the potential is one dimensional and time dependent. As shown in the Poincaré section of figure 4(*a*), an orbit with initial conditions $x_0 = p_{x0} = 1$ fills a large chaotic domain, leaving space only for some small islands of stability. However, if one calculates a Bohmian orbit with the same initial conditions (x_0, p_{x0}), when the ψ-field is an initially minimum uncertainty coherent state centred at (x_0, p_{x0}), this orbit is regular, as indicated by the fall of $\chi(t)$ as $\sim 1/t$ (figure 4(*b*)). This is because the classical system is of one and a half degrees of freedom, while the corresponding quantum system is of one degree of freedom. Therefore, the classical system (20) is chaotic, while the corresponding quantum system is ordered.

As a conclusion, the difference found by Schwengelbeck and Faisal (1995) between the quantum standard map and the quantum cat map is not due to some different intrinsic property of the two maps, but simply to the different dimensions of the ψ-field in these two cases.

At any rate, the main conclusion drawn in this subsection is that a system which is classically integrable (two harmonic oscillators) may have chaotic Bohmian orbits, and vice versa, a system which is classically almost completely chaotic may exhibit no chaos in its Bohmian orbits. It should be noted, however, that the latter case is very improbable in systems

of more than one degrees of freedom. Namely, if a system of two or more degrees of freedom is classically chaotic, its Bohmian orbits, for a generic choice of guiding ψ-field, are likely to be also chaotic.

3.2. Wave packets in Hénon–Heiles Hamiltonians

The example of the previous subsection refers to a choice of the ψ-field corresponding to the extreme case of superposition of a small number (three) of eigenfunctions. Our next example refers to the other extreme case, in which infinitely many eigenfunctions are superposed to form a Gaussian wave packet or coherent state. This case is interesting from two points of view:

(a) As long as the wave packet maintains its coherence, the Bohmian orbits are relatively simple: they just follow the motion of the packet, thus they resemble to the orbits of the Ehrenfest theorem. On the other hand, from the moment when the wave packet loses its coherence, the ψ-field becomes quite irregular. This is reflected in the Bohmian orbits becoming chaotic. Namely, the *same* Bohmian orbit looks regular for a transient period of time, that is equal to the packet's coherence time, while later on the orbit becomes chaotic.

(b) It is well known (Feit and Fleck 1984, Founargiotakis *et al* 1989) that an initially coherent packet may develop quite irregular nodal patterns in a short time period, even when the classical dynamics of the underlying Hamiltonian is close to, or exactly, integrable. In this case too we can speak about chaos as a genuine quantum phenomenon, that is, not related to the chaos of classical dynamics.

In order to study these phenomena, we solve numerically, with a split-step Fourier method (Feit *et al* 1982), the 2D time-dependent Schrödinger equation (equation (1)) for the non-integrable Hénon–Heiles Hamiltonian:

$$H = \tfrac{1}{2}\left(p_x^2 + p_y^2\right) + \tfrac{1}{2}(x^2 + y^2) + \lambda x\left(y^2 - \tfrac{1}{3}x^2\right) \tag{23}$$

with $\lambda = 0.111\,8034$ as in Feit and Fleck (1984), setting as initial condition of the ψ-field a minimum uncertainty wave packet

$$\psi(x, y, 0) = \exp\left(-\tfrac{1}{2}[(x - x0)^2 + (y - y0)^2 + \mathrm{i}(p_{x0}x + p_{y0}y)]\right). \tag{24}$$

According to Ehrenfest's theorem, this packet moves for a short period of time preserving its shape, with the centre of mass moving along a classical orbit in the respective Hamiltonian with initial conditions $(x_0, y_0, p_{x0}, p_{y0})$. If $\lambda = 0$, in the Hamiltonian (24), the packet remains coherent for an infinitely long time. On the other hand, if $\lambda \neq 0$ the packet is expected to lose its coherence within a finite time. An example is shown in figure 5, referring to wave packets of the form (25) in the Hamiltonian (24) with initial conditions

$$x_0 = y_0 = p_{x0} = p_{y0} = \frac{\rho}{2}$$

and $\rho = 1.3$ (figure 5(a)), $\rho = 2$ (figure 5(b)) and $\rho = 3$ (figure 5(c)). These panels show the evolution of the respective wave packets at three different time snapshots. The wave packet for $\rho = 1.3$ (figure 5(a)) partly maintains its coherence up to the time of the last plotted snapshot, $t = 270$. At $t = 180$, the packet splits in two parts, which are later joined again ($t = 270$). This splitting and rejoining of the packet is repeated a number of times after $t = 270$. For ρ larger ($\rho = 2$, figure 5(b)), the initial packet develops a number of new maxima already at time $t = 90$. The structure formed shows rotation as a whole ($t = 180$), while it also merges from time to time to an apparently unique maximum (e.g., at $t = 270$). Finally, for ρ still larger ($\rho = 3$, figure 5(c)), the packet splits quickly by developing a number of local maxima joined by a quite irregular nodal pattern.
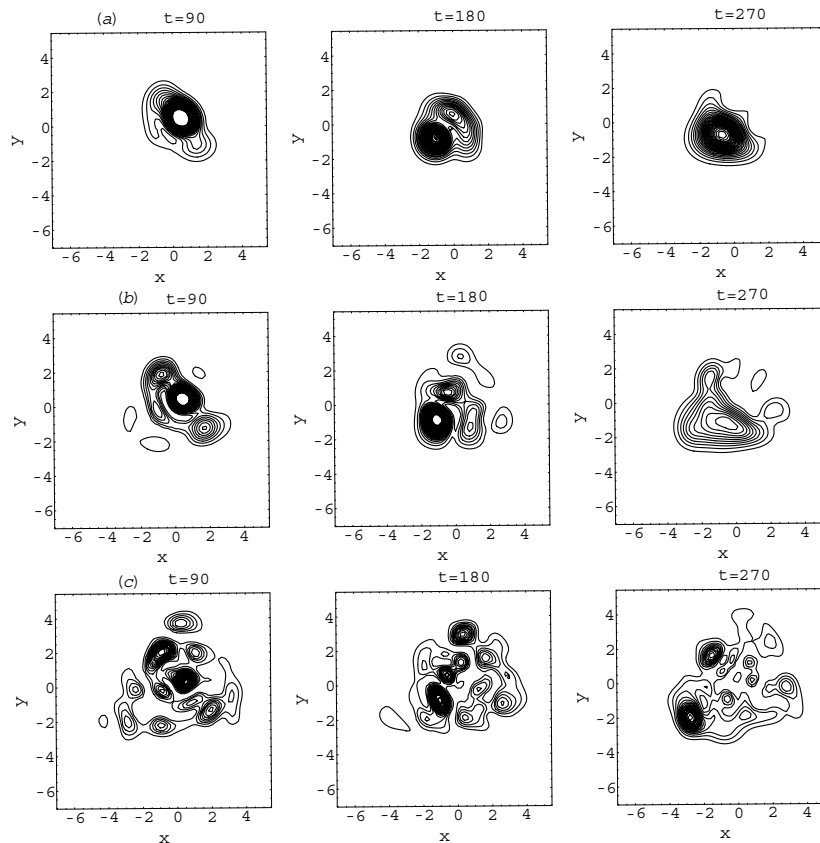
Figure 5. Time evolution of the wave packets given by the initial conditions of equation (24) in the Hamiltonian (23), for (a) $\rho = 1.3$, (b) $\rho = 2$ and (c) $\rho = 3$. The three panels in each row correspond to three different time snapshots $t = 90$, $t = 180$ and $t = 270$.

Figures 6(a)–(c) show the Poincaré surfaces of section $(x, \dot{x} \equiv p_x)$ for $y = 0$, $\dot{y} > 0$ corresponding to the classical Hamiltonian equations of motion with energy equal to $E = H(x_0, y_0, p_{x0}, p_{y0})$, where $(x_0, y_0, p_{x0}, p_{y0})$ are chosen as in figures 5(a)–(c) respectively. The main remark here is that in all three cases the classical Poincaré surfaces of section are filled with invariant curves and no appreciable chaos is visible. In fact, some chaos exists in all three cases since the Hamiltonian (23) is not integrable. However, this chaos is located only on very thin layers that correspond to the homoclinic tangle formed by the unstable manifolds of Poincaré–Birkhoff chains of unstable periodic orbits. These chaotic layers resemble to separatrices, but with some width not visible in the scale of figures 6(a)–(c). It follows that the splitting of the wave packets, resulting in the gradual loss of coherence observed in figure 5, cannot be assigned to a chaotic mechanism in the corresponding classical dynamics.

Now, returning to Bohmian mechanics, figures 7(a) and (b) show the Bohmian orbit with initial conditions (x_0, y_0) as in the wave packet of figure 5(a), for a short time ($t \leqslant 200$, figure 7(a)) and long time ($t \leqslant 1000$, figure 7(b)), respectively. Since the pilot-wave equations (2) are first-order ODEs, the initial positions (x_0, y_0) are the only required initial conditions. Nevertheless, substitution of the wave packet (equation (24)) into the pilot-wave equations yields the initial velocities of the respective Bohmian orbits $(\dot{x}_0, \dot{y}_0) = (p_{x0}, p_{y0})$, which are precisely the same initial conditions as in the classical equations of motion.
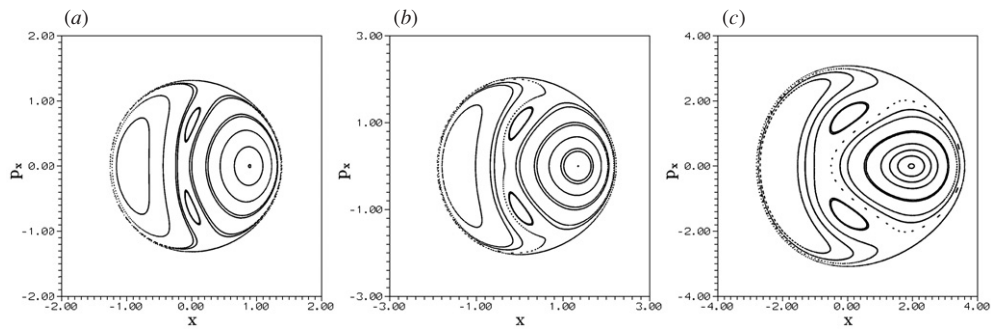
Figure 6. Poincaré surfaces of section $(x, \dot{x} \equiv p_x)$ for $y = 0$, $\dot{y} > 0$ corresponding to the classical Hamiltonian equations of motion with energy equal to $E = H(x_0, y_0, p_{x0}, p_{y0})$, where $(x_0, y_0, p_{x0}, p_{y0})$ are chosen as in figures 5(a)–(c), respectively.
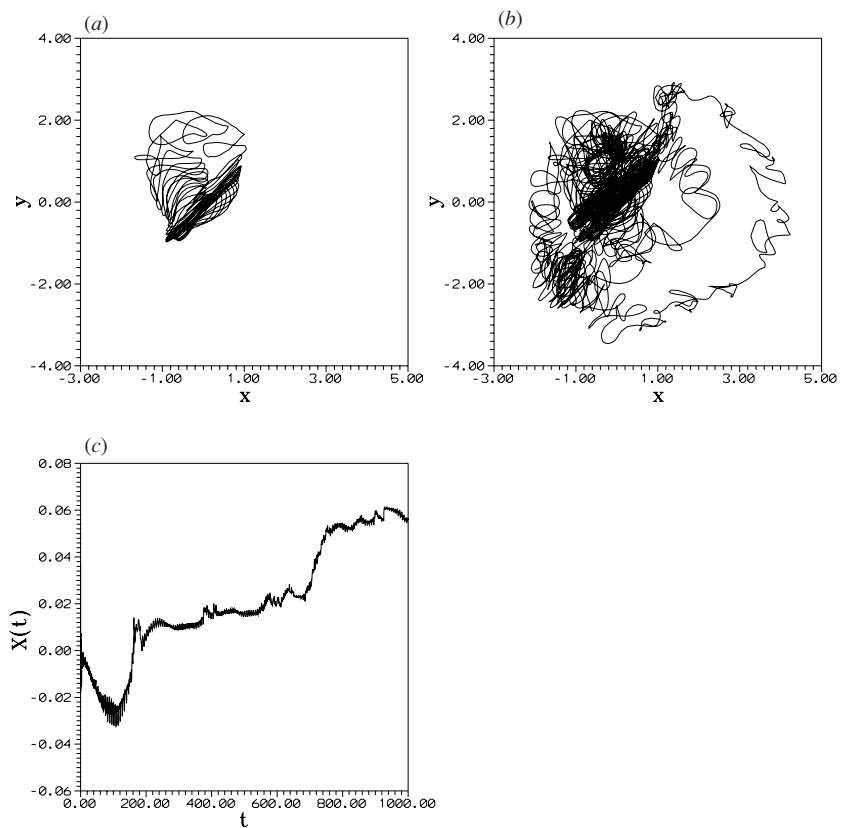

Figure 7. A Bohmian orbit with initial conditions $x_0 = y_0 = \rho/2$ with $\rho = 1.3$ in the guiding field corresponding to the wave packet of figure 5(a). (a) The orbit for $t \leqslant 200$, (b) the orbit for $t \leqslant 1000$ and (c) the time evolution of $\chi(t)$ for the solution of the variational equations with initial conditions $\delta x_0 = 1$, $\delta y = 0$.

The main phenomenon seen in figures 7(a) and (b) is the increasingly irregular shape acquired by the respective Bohmian orbit as its guiding packet gradually loses coherence. Thus, the orbit looks like a regular orbit for a transient time interval ($t \leqslant 200$), while
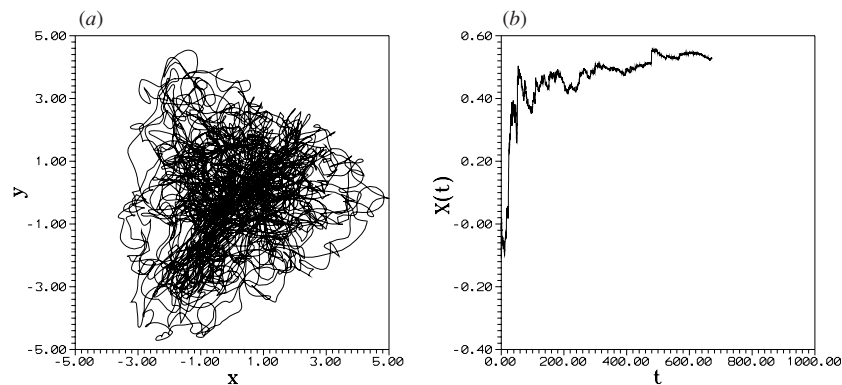
Figure 8. (*a* and *b*) Same as in figures 7(*b*) and (*c*), for the Bohmian orbit with initial conditions $x_0 = y_0 = \rho/2$ with $\rho = 3$ in the guiding field corresponding to the wave packet of figure 5(*c*).

later the orbit starts spreading chaotically and explores a much larger area in configuration space. A calculation of the LCN shows that this orbit is chaotic. In fact, the quantity $\chi(t)$ (figure 7(*c*)) tends to a positive value at the end of the numerical integration ($t = 1000$). However, before reaching this value, $\chi(t)$ undergoes a number of jumps from an initially low value to progressively larger values. Such jumps take place at particular times corresponding to the moments when the respective guiding packet undergoes a splitting. For example, the first jump of $\chi(t)$ in figure 7(*c*) corresponds to the splitting of the respective guiding packet at $t = 180$ (figure 5(*a*)), while a second jump (at $t = 750$) corresponds to a new splitting of the same packet that is not plotted in figure 5(*a*). This behavior of the Bohmian orbit, that looks regular for a transient time interval and then becomes chaotic, is similar to the classical phenomenon of *stickiness*. Classical sticky orbits look like regular orbits that remain close to the borders of an island of stability for quite long times, being obstructed by cantori, i.e., invariant sets of phase space that constitute partial barriers to chaotic diffusion (see Meiss (1992) and Contopoulos (2004) for reviews and Efthymiopoulos *et al* (1997)).

Stickiness in wave-packet dynamics, caused by classical cantori, has been observed by Kollmann and Capel (1997). The stickiness time in this case, where the underlying classical dynamics is nearly integrable, should be distinguished from the decoherence time in kicked rotor models (e.g., Berman and Zaslavsky (1978)), where the underlying classical dynamics is fully chaotic. The fact that Bohmian orbits are also subject to stickiness is crucial as regards the application of the Bohm–Vigier theory, because stickiness implies that this theory is applicable only after the stickiness time is over. In fact, before this time an orbit cannot explore the whole available space, therefore it does not satisfy the necessary conditions of the Bohm–Vigier theory. This point is demonstrated by specific numerical examples in section 4.

Now, as the effective perturbation, quantified by ρ, increases, the transient phenomena disappear and the Bohmian orbits are chaotic from the start. Such is the case of the Bohmian orbit of figure 8, guided by the wave packet of figure 5(*c*) that loses its coherence after a very short time interval. In this case, the quantity $\chi(t)$ (figure 8(*b*)) also tends quickly to a final positive value.

3.3. A modified two-slit experiment

A model for the guiding field $\psi(x, z, t)$ in the usual quantum two-slit experiment is the solution of the initial value problem for the two-dimensional time-dependent Schrödinger equation

$$-\frac{1}{2}\left(\frac{\partial^2\psi}{\partial x^2} + \frac{\partial^2\psi}{\partial z^2}\right) = i\frac{\partial\psi}{\partial t} \tag{25}$$

with initial condition

$$\psi(x, z, 0) = \psi_1(x, z) + \psi_2(x, z) \tag{26}$$

where the functions ψ_i, $i = 1, 2$ are given by

$$\psi_i(x, z) = \psi_{ix}(x)\psi_{iz}(z) = c\exp(ik_x x)\exp\left(\frac{-(z - z_i)^2}{2\sigma_0^2}\right) \tag{27}$$

with $k_x, c, z_i\sigma_0$ being the real constants. The constants z_1, z_2 correspond to the positions of the two slits, c is a normalization constant and k_x is the wave number of the plane wave ψ_{ix} corresponding to a propagation velocity $u = k_x$. The wavefunctions ψ_{iz} are Gaussian functions with dispersion σ_0. These admit the Fourier decomposition

$$\psi_{iz}(z) = \frac{1}{2\pi}\int_{-\infty}^{\infty} c_k\exp(ik(z - z_i))\,dk \tag{28}$$

where

$$c_k = \frac{1}{2\pi}\int_{-\infty}^{\infty}\psi_{iz}\exp(-ik(z - z_i))\,dz. \tag{29}$$

Equation (29), using equation (27), yields

$$c_k \propto \exp\left(-\tfrac{1}{2}k^2\sigma_0^2\right). \tag{30}$$

The solution of the time-dependent Schrödinger equation (equation (25)), for each of the functions ψ_i, $i = 1, 2$, is given analytically in terms of the Fourier coefficients c_k. One has

$$\psi_i(x, z, t) = e^{i(k_x x - E_x t)}\frac{1}{2\pi}\int_{-\infty}^{\infty} c_k\exp(i(k(z - z_i) - E_z t))\,dk \tag{31}$$

where $E_x = k_x^2/2$, $E_z = k^2/2$, yielding

$$\psi_i(x, z, t) \propto e^{i(k_x x - E_x t)}\frac{1}{\sqrt{\sigma_0 + it/\sigma_0}}\exp\left(\frac{-(z - z_i)^2}{2(\sigma_0^2 + it)}\right). \tag{32}$$

Thus, the probability distribution $|\psi_{iz}|^2$ is Gaussian at all times with dispersion

$$\sigma_P^2(t) = \frac{\sigma_0^4 + t^2}{2\sigma_0^2}, \tag{33}$$

i.e., the dispersion increases as the time t increases.

If the distance between the two slits is large enough, $|z_1 - z_2| = \Delta z \gg \sigma_0$, the two Gaussian distributions are initially well separated. However, as the time t increases, the dispersion increases, the two wavefunctions start overlapping and the total wavefunction shows interference. Philippidis *et al* (1979) found that the Bohmian orbits deviate from straight rays so as to be guided to follow the interference pattern created by the ψ-field. This is shown in figure 9. The parameter values are $z_1 = 20$, $z_2 = -20$, $\sigma_0 = 2$ and $k_x = u = 1$. Interference becomes important when the two wavefunctions start overlapping, after a time equal to about $t = 25$ (figure 9(a)).

As t increases, the two wavefunctions overlap in a wider interval Δz. Thus, the consecutive maxima and minima of the interference pattern become visible to a larger extent in the z-axis (compare figures 9(a)–(d) for $t = 25$, $t = 50$, $t = 75$ and $t = 100$, respectively). This remark is crucial as regards the characterization of orbits as regular, or chaotic, because it implies that
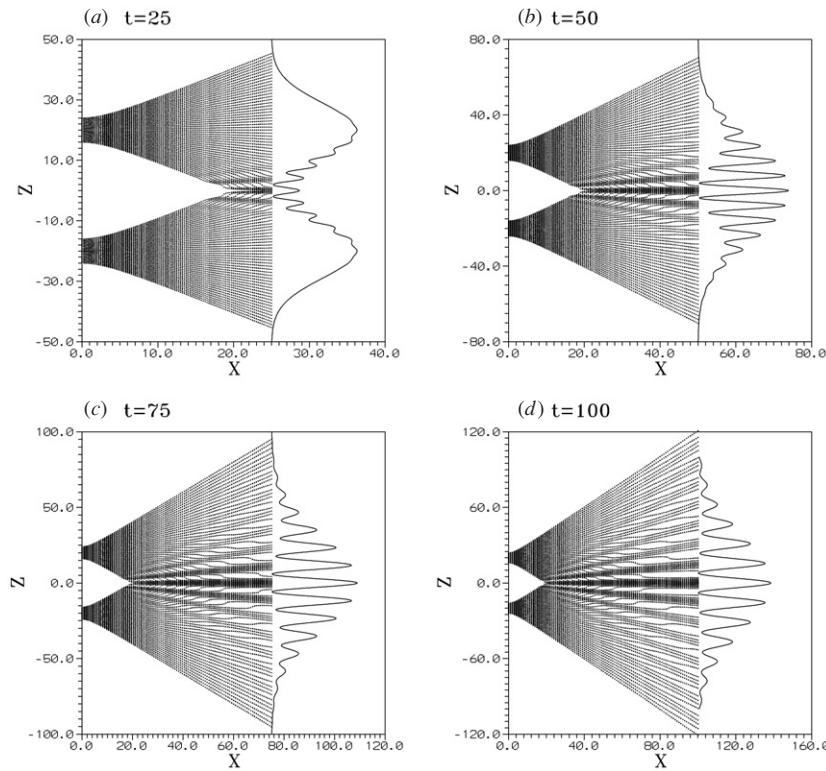
Figure 9. Bohmian orbits in the two-slit experiment. 50 orbits in each slit, with initial conditions uniformly distributed in the interval $z_i - \sigma_0/2 \leqslant z \leqslant z_i + \sigma_0/2$, $i = 1, 2$, with $z_1 = 20$, $z_2 = -20$, $\sigma_0 = 2$, and ψ-field given by the solution of equation (1) for initial condition given by equation (26), with $x = k_x t$, $k_x = 1$. (a) $t = 25$, (b) $t = 50$, (c) $t = 75$ and (d) $t = 100$.

the phase space is not compact in either the x- or z-axis. In fact, the pilot-wave equations, deduced from (2), are

$$\frac{\mathrm{d}x}{\mathrm{d}t} = k_x \tag{34}$$

$$\frac{\mathrm{d}z}{\mathrm{d}t} = -\mathrm{Im}\left(\frac{(z - z_1)\exp\left(\frac{-(z-z_1)^2}{2(\sigma_0^2 + \mathrm{i}t)}\right) + (z - z_2)\exp\left(\frac{-(z-z_2)^2}{2(\sigma_0^2 + \mathrm{i}t)}\right)}{\exp\left(\frac{-(z-z_1)^2}{2(\sigma_0^2 + \mathrm{i}t)}\right) + \exp\left(\frac{-(z-z_2)^2}{2(\sigma_0^2 + \mathrm{i}t)}\right)} \right). \tag{35}$$

Thus, the two equations are uncoupled and they should be examined separately. equation (34) has the trivial solution $x = x_0 + k_x t$. Thus, the only non-trivial equation is (35), which is a time-dependent first-order nonlinear differential equation. This is equivalent to a system of two autonomous nonlinear first-order differential equations, and, as already stressed, there cannot be chaos in such a system.

But even if a coupling is introduced between equations equations (34) and (35), one can still not speak of chaos, because of the non-compactness of phase space. To demonstrate this, we consider a modified two-slit experiment, in which the initial wave fronts form an angle ϕ, for slit 1, and $-\phi$, for slit 2, respectively. That is, the initial wavefunction is

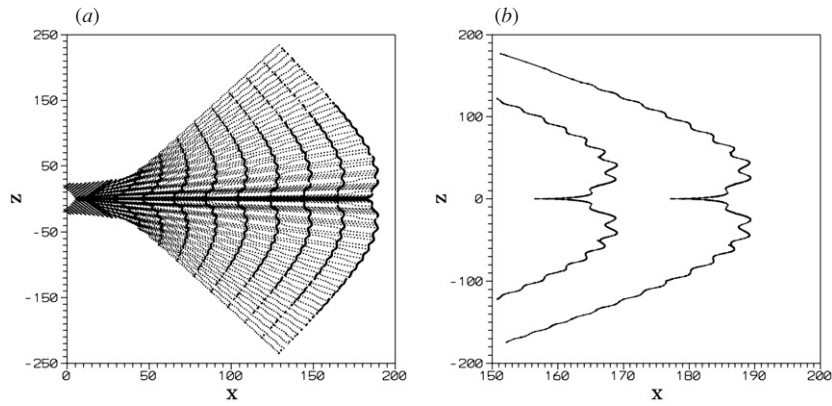$$\psi(x, z, 0) = \psi_1(r_1, y_1, 0) + \psi_2(r_2, y_2, 0) \tag{36}$$

Figure 10. (*a*) Bohmian orbits and the fronts defined by their endpoints in the modified two-slit experiment with $\phi = -0.5$ rad. The fronts are plotted in ten different snapshots $t = 20, 40, \ldots, 200$. (*b*) A magnification of the fronts for $t = 180$ (left curve) and $t = 200$ (right curve).

where ψ_1 and ψ_2 are of the form (27), and

$$r_1 = x \cos\phi + (z - z_1) \sin\phi, \qquad y_1 = -x \sin\phi + (z - z_1) \cos\phi$$

and similarly for (r_2, y_2), with ϕ replaced by $-\phi$ and z_1 replaced by z_2.

Now the two Bohmian equations of motion are coupled, and the coupled system is a system of two non-autonomous, nonlinear first-order ODEs that may in principle exhibit chaos. However, the fact that the phase space is non-compact means that the usual notion of chaos does not apply to these orbits. In particular, as explained in section 2, the calculation of a zero or positive Lyapunov characteristic number does not imply that an orbit is regular or chaotic.

Even so, some mixing can in principle take place in configuration space, on a coarse level, as a result of the quite intricate shape of the curves formed in configuration space by the endpoints of many Bohmian trajectories starting along two initial straight lines (figure 10). In the usual two-slit experiment, the angle ϕ in equation (37) is $\phi = 0$, that is the slits are on the same line $x = 0$. Furthermore, all the points move with constant velocity k_x in the x-axis. Therefore, the image of the initial line $x = 0$ under the Madelung flow, after time t, is simply a new line $x = k_x t$. This is clearly seen in figure 9, for $k_x = 1$. Namely, the endpoints of the orbits, at time t, are all on the straight line $x = t$. If however, $\phi \neq 0$, the points of the first slit are initially on a straight line forming an angle ϕ with the z-axis, while the points of the second slit are on a straight line forming the opposite angle $-\phi$. In fact, one may join these lines continuously by considering the level line of constant phase $S(x, z, 0) = \text{Im}(\text{Log }\psi(x, z, 0)) = \text{const}$, that passes from the slit centres. If $z_2 - z_1 \gg \sigma_0$, the line of constant phase practically coincides, in the neighbourhood of the two slits, with straight lines of inclination angles ϕ and $-\phi$, respectively.

Figure 10(*a*) shows the evolution of the images of these straight segments, that we call 'fronts', in the case $\phi = -0.5$ rad, for ten different time snapshots $t = 20, 40, \ldots, 200$, with initial conditions distributed with a Gaussian distribution along the segment centred at the corresponding slit. A number of Bohmian orbits generating the fronts are overplotted. Clearly, as t increases, the fronts are no longer straight lines, but they develop oscillations around inclined straight segments. Such oscillations are shown in detail in figure 10(*b*), which is a magnification of figure 10(*a*) for the fronts corresponding to the time snapshots $t = 180$

and $t = 200$. Now, since the Bohmian orbits do not cross each other, there cannot be any mixing of Bohmian orbits *along* the front curves. However, one still has to examine whether the oscillations made by these lines can cause any mixing of the orbits on a coarse level. As shown in the next section, this does not happen. Therefore, the Bohm–Vigier theory is not applicable to the two-slit or modified two-slit experiment, because there is no chaotic mixing.

4. Numerical test of the Bohm–Vigier theory and quantum Nekhoroshev stability

As mentioned in the introduction, one main reason why the study of chaos is important in Bohmian mechanics is the fact that chaos may explain the irregularity of the Madelung flow in a quantum system (Bohm and Vigier 1954) without reference to any external mechanism (Bohm 1953), such as collisions of the Bohmian particles or fluid elements with particles or fields not belonging to the system. Furthermore, the irregularity of Madelung's flow is a necessary condition for the applicability of the Bohm–Vigier theory, that an arbitrary initial particle distribution P tends asymptotically to the wavefunction distribution $|\psi(\mathbf{x}, t)|^2$. In the present section, we numerically investigate the applicability of the Bohm–Vigier theory in various quantum systems, as related to the regular or chaotic character of the corresponding Bohmian orbits.

4.1. Bohm–Vigier theory in time-dependent wave packets

Our first example refers to time-dependent wave packets as in subsection 3.2. According to Madelung (1926), if we consider an initial distribution of Bohmian particles of the form $P(x, y) = |\psi(x, y)|^2$ the distribution $P(x, y, t)$ should coincide with $|\psi(x, y, t)|^2$ at any later time t. This property can be used as a test of the accuracy of the numerical integrations of both Schrödinger's equation for the wave packet and of the Bohmian orbits. Such a test is shown in figure 11, in which the initial function $\psi(x, y)$ is given by a Gaussian coherent state (equation (24)). As the numerical calculation is very lengthy, a compromise has to be made as to the number of Bohmian particles in a simulation. Thus, 900 Bohmian orbits are integrated in each experiment. In order to derive a smooth surface density $P_s(x, y, t)$ with only 900 points, a Gaussian smoothing scheme is implemented. Namely, the density P_s is found by imposing a Gaussian kernel to the particles' positions:

$$P_s(x, y, t) = \sum_{i=1}^{900} A \exp\left(-\frac{(x - x_i(t))^2 + (y - y_i(t))^2}{2\sigma_s^2}\right) \tag{37}$$

where the coefficient A is computed so as to render the total probability equal to unity over the grid domain where Schrödinger's equation is solved. The particles are given random initial positions from a Gaussian random generator with dispersion as in the wave packet (24), with initial conditions corresponding to $\rho = 2$ in the Hénon–Heiles Hamiltonian (23). Theoretically the two densities should be equal, $P_s = |\psi|^2$, at any time t. However, due to the numerical noise effects, P_s and $|\psi|^2$ turn out to be only nearly equal. This is demonstrated in figure 11, where the left panels in each column correspond to contour lines of P_s given by equation (37) for the Bohmian particles, while the right panels correspond to contour lines of $|\psi|^2$ at the same time snapshots $t = 30, 60, \ldots, 300$.

The resemblance of the two distributions is visually clear at all times, although the particles' distribution shows more graininess than the $|\psi|^2$ distribution which is derived from a smooth function. The closeness of the two distributions can be quantified in the following
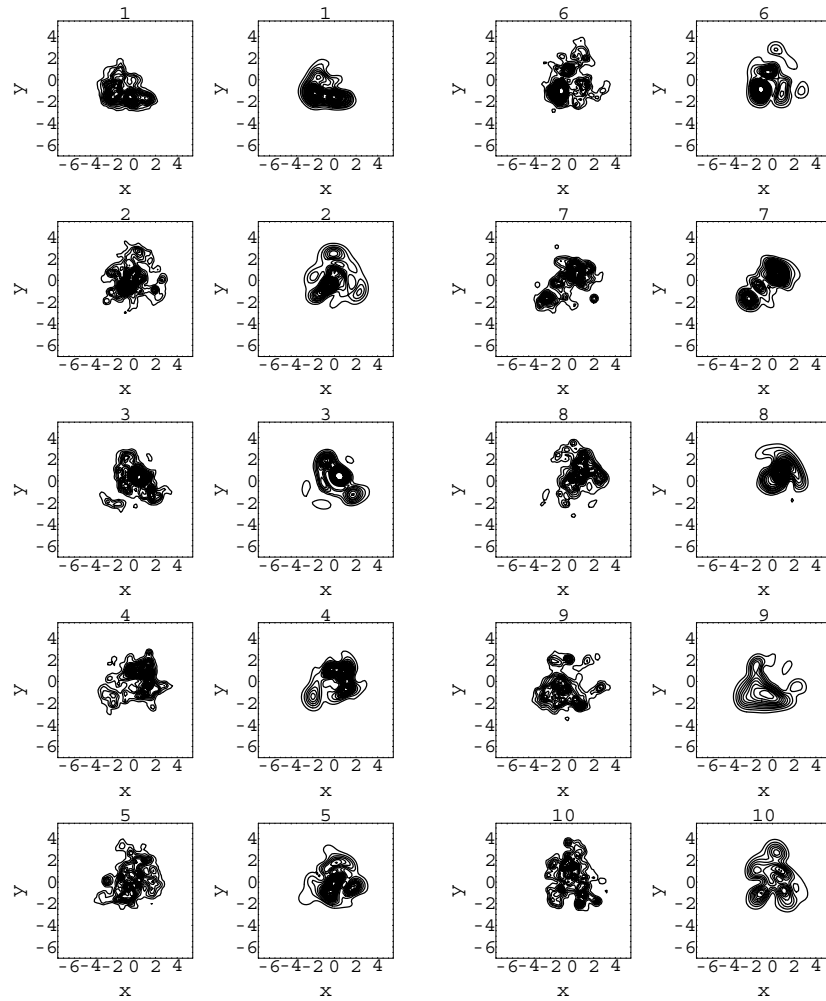
Figure 11. The panels numbered 1–10 show the comparison between the particle density P_s (left column) versus $|\psi|^2$ (right column) in ten time snapshots $t = 30, 60, \ldots, 300$ respectively, for the same experiment as in figure 5(b) (Hénon–Heiles Hamiltonian, $\rho = 2$). The density P_s is given by equation (37) for 900 Bohmian orbits with initial conditions following a Gaussian distribution $|\psi(x, y, 0)|^2$ where $\psi(x, y, 0)$ is the coherent state given by equation (24).

manner: we consider a density difference $D(t)$ given by the sum of absolute differences of the two probability densities over the $N \times N$ grid points (x_k, y_l)

$$D(t) = \sum_{k=1}^{N} \sum_{l=1}^{N} |P_s(x_k, y_l, t) - P(x_k, y_l, t)|, \tag{38}$$

where $P = |\psi|^2$. The grid size is $\mathrm{d}x = (x_{\max} - x_{\min})/N, \mathrm{d}y = (y_{\max} - y_{\min})/N$, with $N = 128$, $x_{\min} = y_{\min} = -12.8$ and $x_{\max} = y_{\max} = 12.8$. Figure 12(a) shows the time evolution of the quantity $D(t)$ in the experiment of figure 11. Initially, the function $D(t)$ has values in the level $D(t) \simeq 3.5$. However, as the system responds to the numerical integrator, $D(t)$ increases, reaching values at the level $D(t) \simeq 10$. At this level, $D(t)$ stabilizes. The statistical significance of this error can be deduced from a simple calculation. Down to the
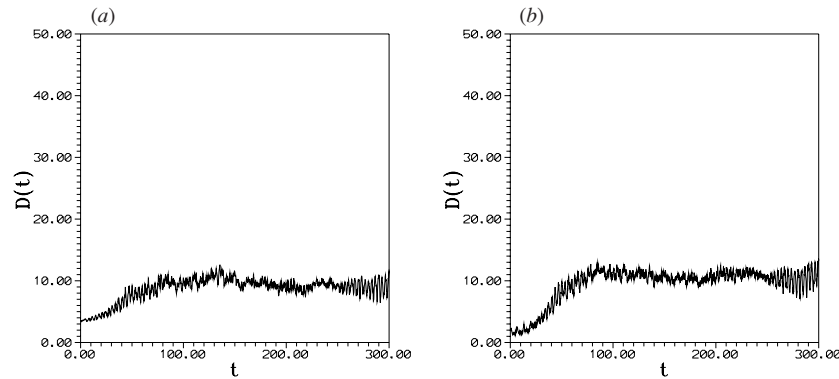
Figure 12. (*a*) The density difference $D(t)$ (equation (38)) for the experiment of figure 11. (*b*) The density difference $D(t)$ in the same experiment, but with 90 000 particles. The particle density P_s is calculated without smoothing.

3-sigma level, the functions P_s and $|\psi|^2$ cover about $\sim$1500 cells in the grid surface. The mean value of P in these cells is $P \sim 0.06$. On the other hand, the mean difference per cell is about $10/1500 = 0.006$. Thus, the mean fractional difference of the values of P and $|\psi|^2$ is of order 10%. Now, this is much less than the expected Poisson noise without smoothing of the density. In fact, without the smoothing kernel, the covering of an area of 1500 cells by 900 particles would imply less than one particle per cell, which would make noise more important than signal. To demonstrate the effectiveness of the smoothing process, figure 12(*b*) shows the function $D(t)$, without smoothing, in an experiment with the same initial conditions as in figure 12(*a*) but with a much larger number of particles (90 000). The evolution of the function $D(t)$ is quite similar in both experiments, although the second experiment uses a much larger number of particles. In fact, the Poisson noise in this latter experiment corresponds to $\sim 1/\sqrt{n_{\text{cell}}}$, where $n_{\text{cell}} = 90\,000/1500 = 60$ is the average number of particles per cell. Thus, the noise is about 13%, that is quite similar to the 10% error found with only 900 particles and a smoothed distribution.

We now check the Bohm–Vigier theory by changing the initial particle distribution P_s so as to have a different distribution from $|\psi|^2$. To this end, we consider an initially homogeneous particle distribution in a square of size $\Delta x = \Delta y = 0.2$, centred at (x_0, y_0) given by the initial conditions of the same wave packet as in figure 11. Figure 13 shows the evolution of the densities P_s and $|\psi|^2$ in this experiment. Clearly, as long as the wave packet remains coherent to some extent, the distribution P_s also maintains its coherence and it is quite different from $|\psi|^2$. However, as $|\psi|^2$ gradually loses its coherence, the particle distribution P_s changes dramatically and gradually obtains the overall shape of $|\psi|^2$. As a result, the two distributions become very similar at $t = 300$.

The degree of similarity of the two distributions can be quantified by plotting the density difference $D(t)$ (figure 14). Initially, the difference $D(t)$ fluctuates around a value $D(t) = 35$ that grows a little later to $D(t) = 45$. This is four times larger than the minimum error level as calculated by the Gaussian distributions. The difference $D(t)$ starts decreasing around $t = 100$. The decrease is rather abrupt and leads to a low value of $D(t)$ around the minimum error level $D(t) = 10$. A further decrease of $D(t)$ cannot be detected with the resolution of the present experiment.

Now, the key point in the above experiment is the remark that the transition value ($t = 100$), when $D(t)$ starts decreasing, is equal to the value of t when the function $\chi(t)$
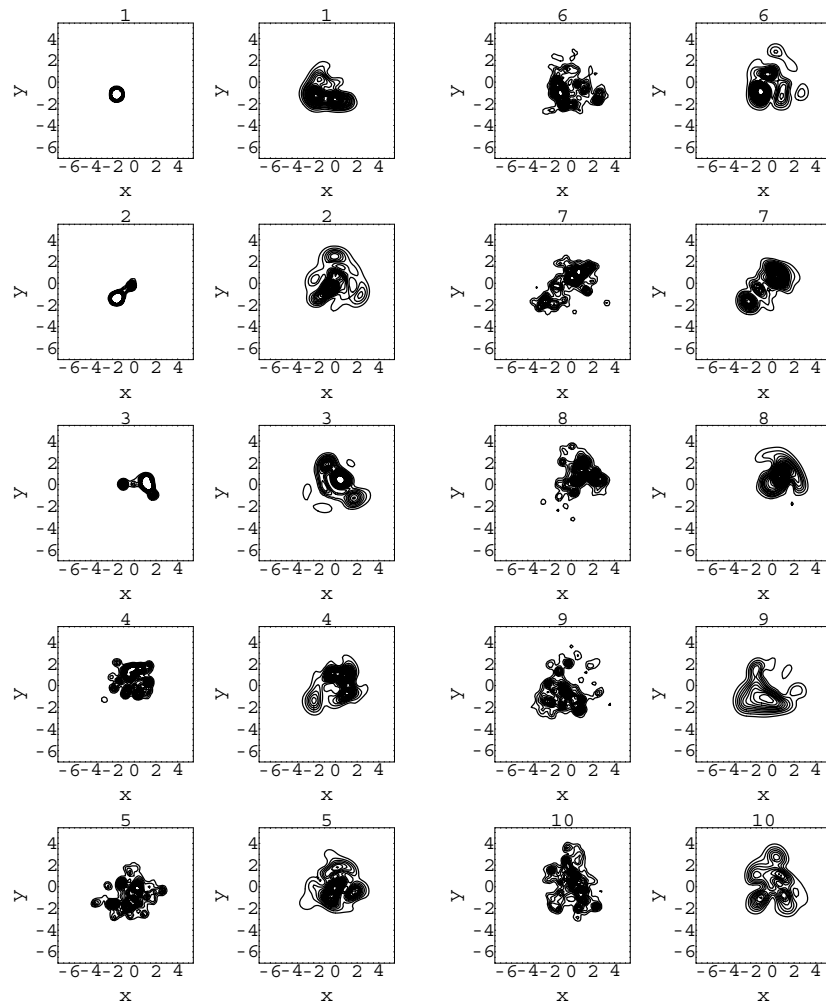
Figure 13. The panels numbered 1–10 show the comparison between the particle density P_s (left column) versus $|\psi|^2$ (right column) in ten time snapshots $t = 30, 60, \ldots, 300$ respectively, for the same experiment as in figure 5(b) (Hénon–Heiles Hamiltonian, $\rho = 2$). The density P_s is given by equation (37) for 900 Bohmian orbits with initial conditions homogeneously distributed in a 0.2×0.2 square centred at $(x_0, y_0) = \rho/2, \rho/2$, with $\rho = 2$, as in figure 5(b).

for a Bohmian orbit starting at the centre of the wave packet (figure 14(b)) shows a first jump to a significantly positive value. That is, the tendency of the two distributions to coincide is related to the degree of chaos of the Bohmian orbits described by the particles forming the distribution P_s.

In order to demonstrate that chaos is responsible for the convergence of P_s to $|\psi|^2$, figure 15 shows the evolution of $D(t)$ in a simpler experiment, namely the two harmonic oscillators Hamiltonian (15) without coupling. The distribution of particles is initially uniform in a square $\Delta x = \Delta y = 0.2$, centred at initial conditions (x_0, y_0) as in the orbits of figures 2 (chaotic) and 3 (regular), respectively. In the case of chaotic orbits, the difference $D(t)$ (curve (a) in figure 15) decreases continuously, albeit rather slowly, from an initial value $D(t) = 40$. On the other hand, in the case of regular orbits (curve (b)), the difference $D(t)$ remains
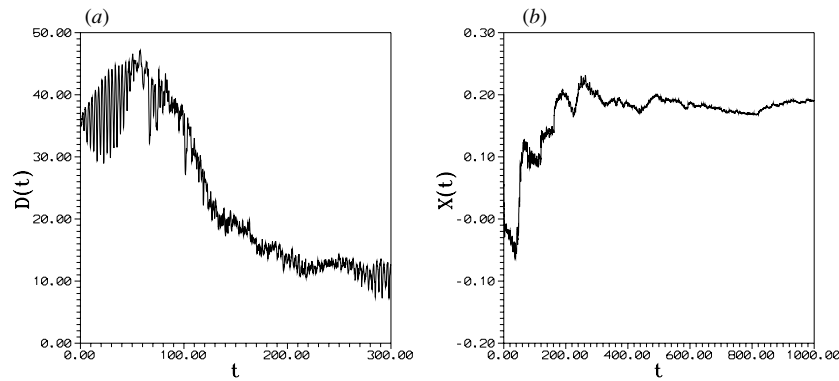
Figure 14. (*a*) The density difference $D(t)$ (equation (38)) for the experiment of figure 13. (*b*) The time evolution of $\chi(t)$ for a Bohmian orbit as in figure 8(*b*), with initial conditions $(x_0, y_0) = \rho/2, \rho/2$, with $\rho = 2$, guided in the ψ-field of figure 13.
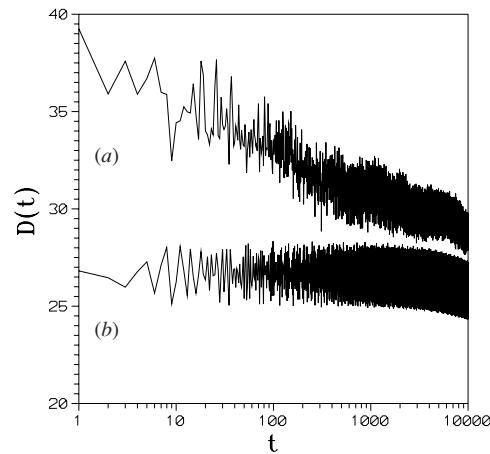

Figure 15. The number density difference $D(t)$ (equation (38)) for 900 Bohmian orbits with initial conditions homogeneously distributed in a 0.2×0.2 square centred at (x_0, y_0), and in the same ψ-field, as (*a*) figure 2(*a*) (chaotic orbit) and (*b*) figure 3(*a*) (regular orbit).

practically constant, up to some noise oscillation, except for a small decrease at the end of the integration. We checked that the final decrease is linear in t, but with a very small slope (8.2×10^{-5}).

The decrease of $D(t)$ in case (*a*), while faster than in case (*b*), is still relatively slow compared to the decrease of $D(t)$ in the case of figure 14(*a*). This should be expected, since the ψ-field has a much simpler form in the present case than in the case of the ψ-field that produces figure 14. This is shown in figure 16, where the particle distribution P_s is compared with the distribution $|\psi|^2$ for the experiment of figure 15(*a*). The distribution $|\psi|^2$ shows a well-defined nodal pattern which is the result of superposition of three stationary states. On the other hand, the particle distribution P_s, which is initially homogeneous in a square around $x_0 = y_0 = 0.1$, quickly splits in two parts (figure 16(*a*), $t = 1$). The left part splits into an upper and a lower part, at $t = 10$ (figure 16(*b*)), while the right part splits a little later (not
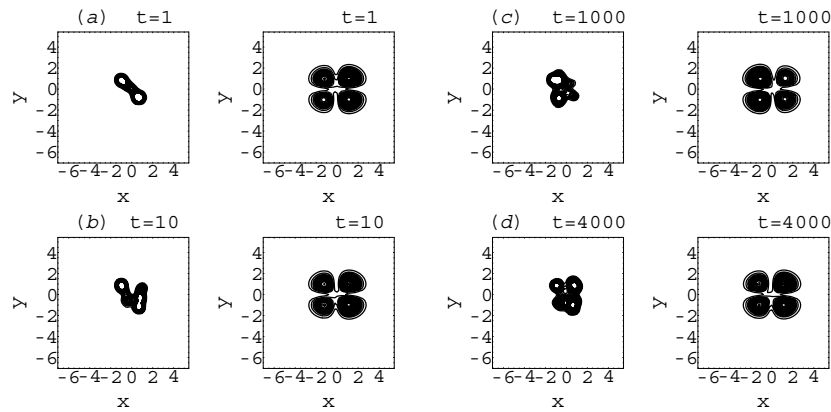
Figure 16. Contour plots of P_s versus $|\psi(x, y, t)|^2$ as in figure 13, when the initial particle distribution is homogeneous in a 0.2×0.2 square around $(x_0, y_0) = (0.1, 0.1)$ and the ψ-field is as in the experiment of figure 2(a). The four time snapshots are (a) $t = 1$, (b) $t = 10$, (c) $t = 1000$ and (d) $t = 4000$.

shown in the figure). However, after these initial splittings, the evolution of P_s towards $|\psi|^2$ slows down (figures 16(c) and (d), for $t = 1000$ and $t = 4000$, respectively).

Returning to the wave packets of the Hénon–Heiles Hamiltonian, figures 17 and 18 are as figures 13 and 14(a), but for initial conditions ($\rho = 1.3$) corresponding to a smaller effective perturbation from the two harmonic oscillators Hamiltonian. The time snapshots are $t = 100, 200, \ldots, 1000$. Clearly, the decoherence of the wave packet, as well as the approach of P_s to $|\psi|^2$, takes place at a much slower rate compared to the experiment of figures 13 and 14. The behaviour of the difference function $D(t)$ is also similar in the two cases, but the time when $D(t)$ starts decreasing, as well as the time it takes for $D(t)$ to reach the error level, is considerably prolonged in the second experiment (compare figures 14(a) and 18).

4.2. A quantum analogue of Nekhoroshev's theorem

By repeating the same experiment for a set of values of ρ, it is possible to obtain estimates of a relation of the form $T(\rho)$, where T is a measure of the timescale of convergence of the distribution P_s to $|\psi|^2$, related to the time of decoherence of the corresponding wave packet, as a function of ρ.

To this end, we define three different measures of T, as demonstrated with the help of figure 19. Figure 19(a) shows the time evolution of $D(t)$ in two experiments ($\rho = 0.5$ and $\rho = 0.8$), for an initial time interval $t \leqslant 2000$. In both cases, the respective functions undergo a number of oscillations such that their values remain within a zone between a maximum and a minimum $D(t)$ for some time. Denoting the variation between maximum and minimum by dP, it is observed that, in the case of the experiment with $\rho = 0.8$, the variations of $D(t)$ remain within a zone dP, with $dP \simeq 4$, for a time $t \leqslant T_{\text{cross}}$, where T_{cross}, the time of crossing of the zone is $T_{\text{cross}} \simeq 800$. On the other hand, in the case of the experiment with smaller ρ ($\rho = 0.5$), the width of the zone is smaller ($dP \simeq 2.5$), but the function $D(t)$ does not cross the respective zone up to $t = 2000$ (the crossing takes place around $T_{\text{cross}} = 4400$. The width of the zone dP is an almost linear function of ρ. In fact, a power-law fit (figure 19(b)) yields the exponent 1.15, that is, very close to unity.
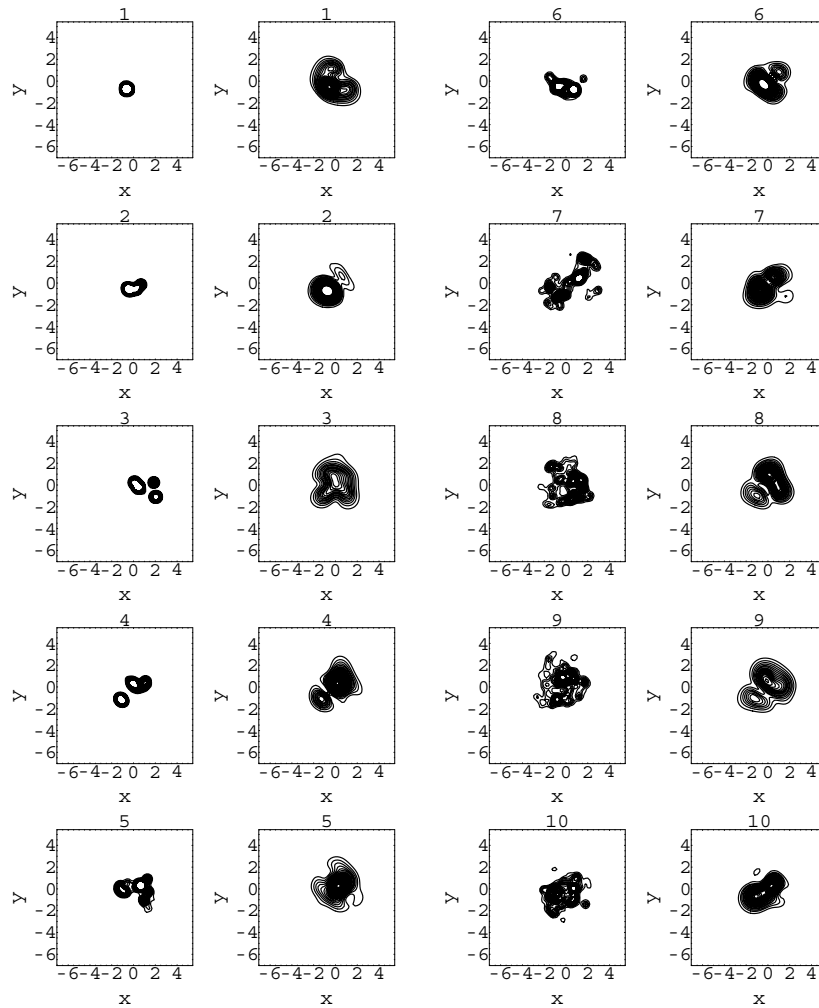
Figure 17. As in figure 13, for a wave packet as in the experiment of figure 5(*a*) (Hénon–Heiles Hamiltonian, $\rho = 1.3$). The ten time snapshots are $t = 100, 200, \ldots, 1000$.

Besides T_{cross}, an independent measure of the time T is provided by the time when $D(t)$ crosses a particular threshold value. Here, we consider the times T_{20} and T_{15} that correspond to the moments when $D(t)$ crosses the values $D(t) = 20$ and $D(t) = 15$, respectively. Both times are much longer than T_{cross}, therefore they both represent the scaling of T with respect to ρ in the long-term dynamics. Furthermore, in order to smooth out short-time variations of $D(t)$, we consider smoothed curves $D(t)$ obtained from the non-smoothed curves by a smoothing average method with time window $\Delta t = 7.5$. Figures 19(*c*) and (*d*) show the non-smoothed and the smoothed curves of the experiments with $\rho = 1.3$ and $\rho = 2$. The time axis is plotted on a logarithmic scale. Then, the times T_{20} and T_{15} are obtained as the last times when the smoothed curves cross the values $D(t) = 20$ and $D(t) = 15$, respectively.

Figure 20(*a*) shows the final result. For a series of experiments in the range of values $0.5 \leqslant \rho \leqslant 2$, the time T, as represented by T_{cross}, or T_{20} and T_{15}, is well fitted by an *exponential law* in the inverse of ρ. Namely, the three curves $\ln T_{\mathrm{cross}}$, $\ln T_{20}$, $\ln T_{15}$ versus $1/\rho$
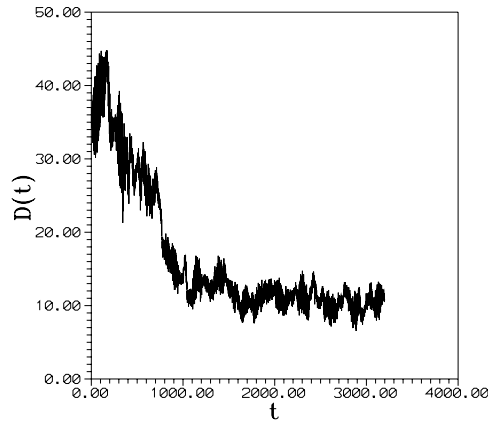
Figure 18. The time evolution of the density difference $D(t)$ (equation (38)) for the experiment of figure 17.
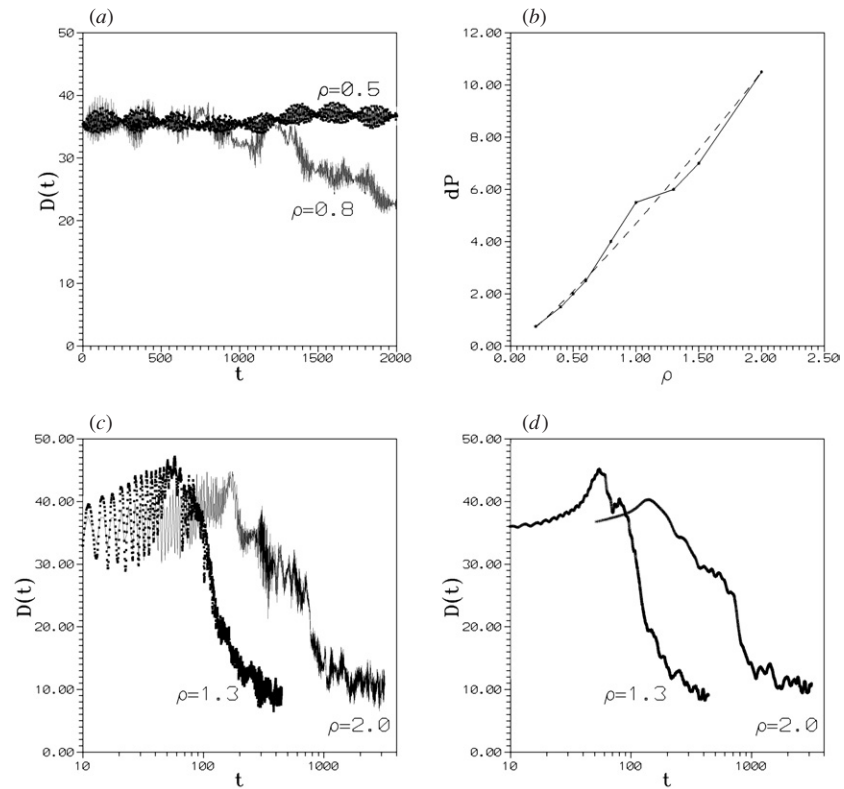

Figure 19. (*a*) The functions $D(t)$ for two experiments corresponding to the values $\rho = 0.5$ and $\rho = 0.8$, for an initial time interval $t \leqslant 2000$. (*b*) The maximum variation dP of $D(t)$ in an initial time interval ($t \leqslant 300$) as a function of ρ and a power-law fit of this function. (*c*) Non-smoothed functions $D(t)$ as in the previous experiments and (*d*) smoothed functions with a moving window of width equal to $\Delta t = 7.5$.
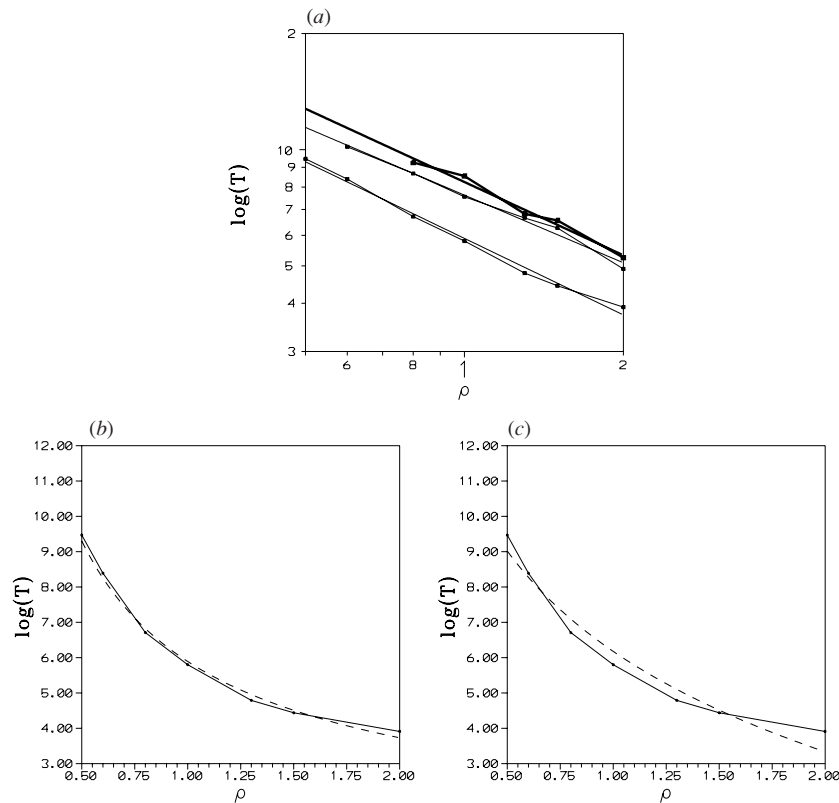
Figure 20. (*a*) The time of wave-packet stability as a function of the effective perturbation ρ. Lower curve: $\log T_{\text{cross}}$ versus ρ. Middle curve: $\log T_{20}$ versus ρ. Upper curve: $\log T_{15}$ versus ρ. (*b*) The curve $\log T_{\text{max}}$ versus ρ in linear scale. The dashed curve is a power-law best fitting curve that corresponds to an exponential scaling of T over ρ. (*c*) Same as (*b*), with a logarithmic best fitting that corresponds to a power-law scaling of T with ρ.

are well fitted by $\ln T \propto (1/\rho)^a$, with similar exponents, $a = 0.659$ for T_{max}, $a = 0.583$ for T_{20}, $a = 0.631$ for T_{15}. Let us note that the time T_{cross} was calculated for all the experiments in the range $0.5 \leqslant \rho \leqslant 2$, while the times T_{20} and T_{15} were not calculated for very small values of ρ, because the function $D(t)$ did not cross the respective thresholds up to the last time of numerical integration. Thus, the curve T_{cross} versus ρ provides the most reliable information. In fact, given the limited range of values of ρ, one may also try other fitting laws. For example, figure 20(*c*) shows a power-law fitting for the same data ($\log T$ is plotted on a linear scale), which is compared to the exponential fitting (figure 20(*b*)) plotted in the same scale. Although the exponential fitting (figure 20(*b*)) is clearly better than the power-law fitting (figure 20(*c*)) for these data, the power law also yields a reasonable fit. We conclude that, quite likely, the time T scales exponentially with $1/\rho$, but experiments for a much longer integration time are required in order to exclude the possibility of a power law.

Exponential stability is a very well-known property of the orbits in classically nearly integrable Hamiltonians, that is the content of the theorem of Nekhoroshev (1977). The result of figure 20 indicates that a quantum version of Nekhoroshev theorem may be applicable to the decoherence times of wave packets in quantum Hamiltonians corresponding to perturbed harmonic oscillators. This time can become very long provided that ρ is small. For example,
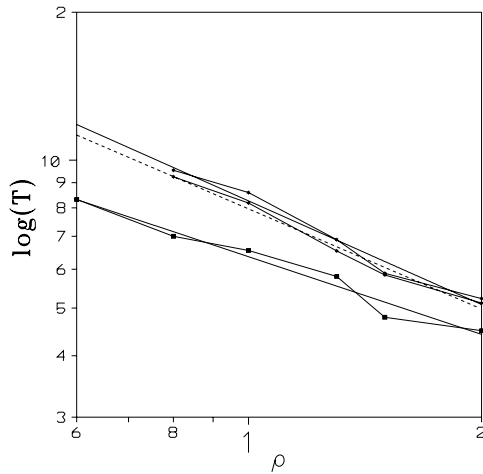
Figure 21. The time of wave-packet stability as a function of the effective perturbation ρ for the Hamiltonian (39). Lower curve: $\log T_{\text{cross}}$ versus ρ. Middle curve: $\log T_{20}$ versus ρ. Upper curve: $\log T_{15}$ versus ρ.

if the curves of figure 20 are extrapolated to a distance ten times smaller than the outermost left point, the time of exponential stability becomes $\exp(10^{0.6}) = 53$ times larger. For ρ smaller by a further factor 10, this time is $\exp(100^{0.6}) = 7.6 \times 10^6$ times larger. Thus, for ρ sufficiently small, the Nekhoroshev time exceeds any dynamical timescale relevant to the quantum system under study. It follows that the convergence of the P and $|\psi|^2$ distributions may require a time that exceeds any timescale of physical interest.

Finally, figure 21 shows the result of a similar calculation in the Hamiltonian

$$H = \tfrac{1}{2}\left(p_x^2 + p_y^2\right) + \tfrac{1}{2}(x^2 + y^2) - 0.024\,8452\,y(x^2 + 2y^2). \tag{39}$$

This Hamiltonian is known to be classically integrable (Bountis *et al* 1982) as well as quantum integrable in the sense of commuting Moyal brackets (Hietarinta 1983). However, the Bohmian orbits in this Hamiltonian exhibit chaos. We have repeated the calculation of LCNs for many orbits guided by a wave packet in this Hamiltonian and found that they are typically positive. Furthermore, as shown in figure 21, the times T_{cross}, T_{20} and T_{15} also appear to scale exponentially with the inverse of the effective perturbation $1/\rho$, with a noticeable difference in the exponent a for the curve T_{cross} versus ρ. In conclusion, it appears that the phenomenon of exponential stability of wave packets is generic in quantum systems that are perturbations of harmonic oscillator systems.

4.3. Testing the Bohm–Vigier theory in a modified two-slit experiment

In the usual two-slit experiment, Bohmian orbits are started at the slit positions, that is with initial conditions $x_0 = 0$ and z_0 in an interval around each slit's centre. On the other hand, a detector is placed in some plane $x = \text{const}$ that counts the arrival of particles to this plane. In order to test the Bohm–Vigier theory, one then has to calculate the linear density along the plane at the time t when particles are incident to it. Numerically, the linear density $P_s(z)$ is calculated as $P_s(z) = \Delta N(z)/\Delta_z$, where $\Delta N(z)/\Delta z$ is the number of particles arriving in a small bin of width Δz centred at z.

Figure 22(a) shows the comparison of the numerical density $P_s(z)$, for a realization of an initially Gaussian distribution $(|\psi(x, z, 0)|^2$ with ψ given by equation (26) and 500
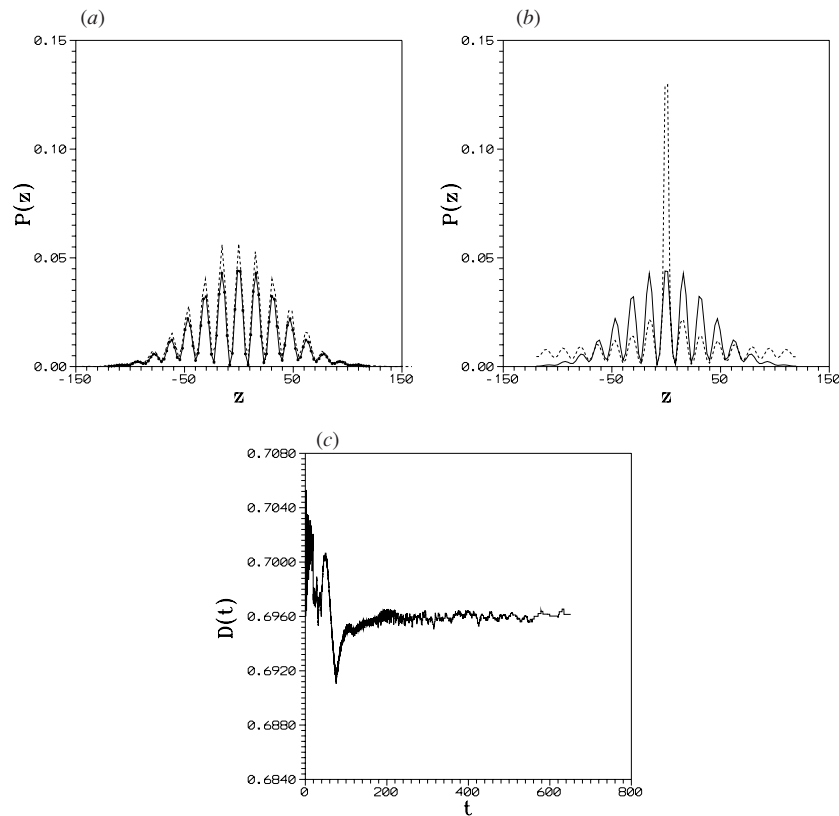
Figure 22. (*a*) Comparison of the numerical density $P_s(z)$ with $|\psi|^2$ in the two-slit experiment. The particles are given initial conditions with two Gaussian distributions ($=|\psi(x, z, 0)|^2$) with ψ given by equation (26) and 500 particles in each slit. The function $P_s(z)$ (dashed curve) is compared with the density $|\psi(x, z, t)|^2$ (solid curve) when $x = k_x t$ and $k_x = 1$, $t = 100$. (*b*) Same as (*a*) for an initially homogeneous distribution of particles $P_s(0)$, while ψ is again given by (26). (*c*) The number density difference as a function of time in the case of experiment (*b*).

particles in each slit, with the density $|\psi(x, z, t)|^2$, as a function of z, on the incidence plane $x = k_x t$, for $t = 100$. As predicted for a Madelung flow, these distributions almost coincide (a small difference in the central peaks is due to the poor sampling of the initial Gaussian particle distribution at its tails). On the other hand, figure 22(*b*) shows the comparison of P_s and $|\psi|^2$ when the initial particle distribution is homogeneous instead of Gaussian. Clearly, the two densities are now different, although the positions of the minima and maxima of both densities coincide. This means that while the orbits guided by the ψ-field produce the correct interference pattern, the resulting intensities on the incidence plane are not the same. In fact, a calculation of the density difference $D(t)$ (figure 22(*c*)) shows that this difference remains constant in time. Here, the function $D(t)$ is calculated simply as $D(t) = \sum_{j=1}^{M} |\Delta N(j)/N - |\psi_j|^2|$, where $j = 1, \ldots, M$ refers to the jth bin and ψ_j is the value of the ψ-field at the centre of the bin. The constancy of $D(t)$ follows trivially from the fact that the Bohmian orbits do not cross (subsection 3.3), therefore any initial difference of the number of particles $\Delta N(z_j)$ in a particular bin Δz_j, at $t = 0$, is preserved in the image of this bin at any later time t.
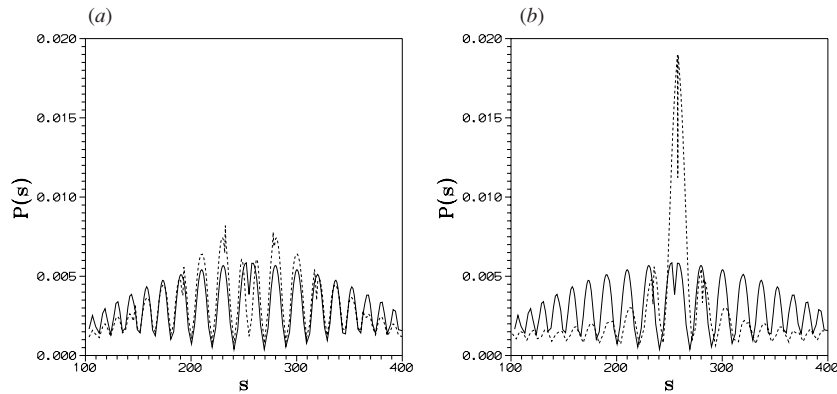
Figure 23. (*a*) Comparison of the particle density $P(s)$ (dashed curve) versus $|\psi|^2$ (solid curve), at time $t = 200$, for an initially Gaussian particle distribution at each slit, in the modified two-slit experiment with $z_1 = 20$, $z_2 = -20$, $\sigma = 2$ and $\phi = -0.5$ rad. The variable s is the length parameter along the fronts of figure 10(*a*). The number of particles is 578 at each slit. (*b*) Same as (*a*), when the initial particle distribution is homogeneous in an interval of width 4σ centred at each slit.

Now, as shown in subsection 3.3, the same property, of non-crossing of the orbits, also holds in the modified two-slit experiment, with $\phi = -0.5$. Therefore, the density difference is expected to remain constant. Numerically, in order to define a linear density in the fronts of figure 10, we approximate these fronts as polygonal lines joining the endpoints of a number of Bohmian orbits (500 in each split) that trace the evolution of the front. Then, the cumulative density $C(s)$, for an initially Gaussian or uniform distribution, is calculated as a function of the length parameter s along a polygonal line. Numerical differentiation of $C(s)$ yields the linear density $P(s)$ as a function of the length parameter s along the front. As shown in figure 23, the same phenomenon takes place as in figures 22(*a*) and (*b*). Namely, when the initial particle distribution is homogeneous, the peaks of $P(s)$ are at the correct place on the incidence front, but they have quite different values than those of $|\psi|^2$. On the other hand, when the initial distribution is Gaussian, the peaks of $P(s)$ are at the correct place and have similar values as the peaks $|\psi|^2$. In fact, a small difference between these values observed for the central peaks is caused by the poor sampling of the initial Gaussian particle distribution near the line $z = 0$ where the fronts coming from the two slits are joined. Similarly, a difference in the high tail of the two distributions is caused by a truncation of the particle distribution that we numerically impose at the 4-sigma level.

The question now arises whether the foldings that are progressively developed on the fronts (figure 10) may cause an equalization of the densities in a coarse level, that is in a zone that determines an area around each front. In order to check this, we considered particles starting in the neighbourhood of each slit, with initial conditions as in figure 10, but r_0 with a uniform distribution in an interval $0 \leqslant r \leqslant \Delta r = \sigma_0$. An *area* density P_s, instead of linear density, is then calculated by the Gaussian smoothing algorithm of equation (37). Figure 24 shows the result of the density difference $D(t)$ when the initial density is (*a*) uniform or (*b*) Gaussian, in the y variable. Clearly, in case (*a*) the difference $D(t)$ stabilizes to a value well above the error level, given by the curve (*b*). That is, the densities P_s and $|\psi|^2$ do not tend to coincide even in a coarse level. This means that the Bohm–Vigier theory is not applicable in the case of the modified two-slit experiment, not even in a coarse grained way, because there is no chaotic mixing.
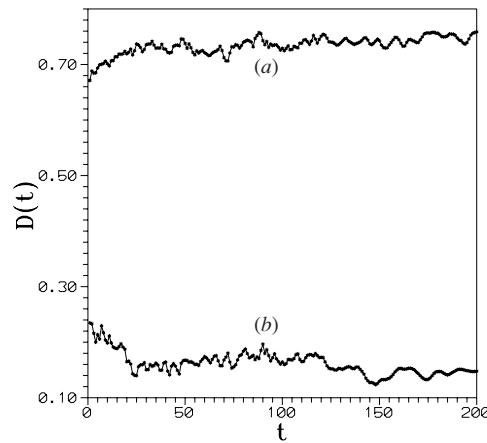
Figure 24. Time evolution of the area density differences $D(t)$ in the modified two-slit experiment with $z_1 = 20$, $z_2 = -20$, $\sigma = 2\phi = -0.5$ rad. The particles (900 at each slit) are given initial conditions with (a) uniform and (b) Gaussian distributions in y centred at the two slits, while they are uniformly distributed in the variable r within the interval $0 \leqslant r \leqslant \sigma_0$.

5. Conclusions

In the present paper, we study chaos in a number of characteristic examples of quantum systems by means of the orbits of the corresponding Bohmian mechanics. We numerically also check the extent of applicability of the Bohm–Vigier theory, concerning the equalization of the particle's P and $|\psi|^2$ distributions, when the irregularity of Madelung's flow is caused by the chaotic character of the associated Bohmian orbits. Our main conclusions are

(1) We discuss necessary conditions that should apply in order to define chaos in time-dependent potentials such as the Bohmian quantum potential. We also describe a method to precisely calculate the Lyapunov characteristic number and point out examples in the literature where this calculation is done by imprecise methods leading to the erroneous characterization of regular orbits as chaotic.

(2) In one-dimensional systems, the Bohmian orbits are always regular, while the classical orbits can be chaotic if the classical potential is time dependent. Bohmian chaotic orbits exist in systems of more than one dimension. This remark explains the difference between the Bohmian orbits in the quantum standard map (regular) and in the quantum Arnold cat map (chaotic).

(3) In simple quantum systems (superposition of three stationary states in two uncoupled harmonic oscillators) with an aperiodic quantum potential, there are both regular and chaotic orbits.

(4) We study the Bohmian orbits in the ψ-field generated by an initially coherent Gaussian wave packet in the Hénon–Heiles Hamiltonian. When the coupling perturbation is nonzero, we always find chaotic orbits. However, the evolution of the function $\chi(t)$ (equation (10)) towards a positive limit (the LCN) is through abrupt jumps. Each jump is linked to a splitting of the corresponding wave packet, which gradually leads to lose its coherence by a number of consecutive splittings. Before the first splitting, the values of $\chi(t)$ are very close to zero, meaning that the orbit effectively behaves as regular. This behaviour is similar to the classical phenomenon of 'stickiness'.

(5) When the Bohmian orbits are chaotic, the distributions P and $|\psi|^2$ tend to coincide asymptotically in time, while, if the orbits are regular, the distributions P and $|\psi|^2$ retain a difference almost constant in time.

(6) The time of decoherence of a wave packet is of the same order as the time of equalization of P and $|\psi|^2$. In the Hénon–Heiles Hamiltonian, this time is well fitted by a fitting law which is exponentially long in the inverse of the effective perturbation (measured by the radius ρ or the associated energy value found from (23), see subsection 3.2). A similar result is found in the case of an integrable Hénon–Heiles Hamiltonian. This result is a quantum analogue of Nekhoroshev theorem of exponential stability in classical Hamiltonian dynamics.

(7) In two-slit or modified two-slit experiments, the phase space is not compact, therefore the usual notion of chaos is not applicable. But the most important thing is that the Bohmian orbits do not cross. As a result, we find no equalization of P and $|\psi|^2$, when viewed either as linear densities on a plane of incidence or surface densities in configuration space. In conclusion, the Bohm–Vigier theory is not applicable in the case of two-slit experiments.

Acknowledgment

References

Aspect A, Delibard J and Roger G 1982 *Phys. Rev. Lett.* **49** 1804
Bell J S 1965 *Phys. (NY)* **1** 195
Bell J S 1976 *Epistemol. Lett.* **9** 11
Bell J S 1987 *Speakable and Unspeakable in Quantum Mechanics* (Cambridge: Cambridge University Press) p 173
Benettin G, Galgani L and Strelcyn J M 1976 *Phys. Rev.* A **14** 2338
Berry M V 1979 *Topics in Nonlinear Dynamics (AIP Conf. Proc.* vol 46*)* ed S Jorna (New York: American Institute of Physics)
Berman G P and Zaslavsky G M 1978 *Physica* A **91** 450
Bohm D 1952a *Phys. Rev.* **85** 166
Bohm D 1952b *Phys. Rev.* **85** 180
Bohm D 1953 *Phys. Rev.* **89** 458
Bohm D and Hiley B J 1993 *The Undivided Universe* (London: Routhledge)
Bohm D and Vigier J P 1954 *Phys. Rev.* **26** 208
Bowman G E 2002 *Phys. Lett.* A **298** 7
Contopoulos G 1960 *Z. Astrophys.* **49** 273
Contopoulos G 1966 *J. Math. Phys.* **7** 788
Contopoulos G 2004 *Order and Chaos in Dynamical Astronomy* (Berlin: Springer)
de Broglie L 1926a *C. R. Acad. Sci., Paris* **183** 447
de Broglie L 1926b *Nature* **118** 441
de Broglie L 1927a *C. R. Acad. Sci., Paris* **184** 283
de Broglie L 1927b *C. R. Acad. Sci., Paris* **185** 380
de Broglie L 1927c *J. Phys.* **8** 225
de Polavieja G G 1996 *Phys. Rev.* A **53** 2059
de Sales J A and Florencio J 2003 *Phys. Rev.* E **67** 016216
Dewdney C 1992 *J. Phys. A: Math. Gen.* **25** 3615
Dewdney C and Malik Z 1993 *Phys. Rev.* A **48** 3513
Dewdney C and Malik Z 1996 *Phys. Lett.* A **220** 183
Dürr D, Goldstein S and Zanghi N 1992a *J. Stat. Phys.* **68** 259
Dürr D, Goldstein S and Zanghi N 1992b *Phys. Lett.* A **172** 6
Efthymiopoulos C, Contopoulos G, Dvorak R and Voglis N 1997 *J. Phys. A: Math. Gen.* **30** 8167
Faisal F H M and Schwengelbeck U 1995 *Phys. Lett.* A **207** 31
Feit M D and Fleck J A 1984 *J. Chem. Phys.* **80** 2578

Feit M D, Fleck J A and Steiger A 1982 *J. Comput. Phys.* **47** 412

Falsaperla P and Fonte G 2003 *Phys. Lett.* A **316** 382

Founargiotakis M, Farantos S C, Contopoulos G and Polymilis C 1989 *J. Chem. Phys.* **91** 1389

Gutzwiller M C 1990 *Chaos in Classical and Quantum Mechanics* (New York: Springer)

Holland P 1993 *The Quantum Theory of Motion* (Cambridge: Cambridge University Press)

Holland P 2005 *Ann. Phys.* **315** 505

Holland P and Philippidis C 2003 *Phys. Rev.* A **67** 062105

Iacomelli G and Pettini M 1996 *Phys. Lett.* A **212** 29

Jammer M 1974 *The Philosophy of Quantum Mechanics* (New York: Wiley) p 265

Keller J B 1953 *Phys. Rev.* **89** 1040

Kochen S and Specker E P 1967 *J. Math. Mech.* **17** 59

Kollman M and Capel H W 1997 *Physica* A **247** 379

Kosloff R and Rice S A 1981 *J. Chem. Phys.* **74** 1340

Madelung E 1926 *Z. Phys.* **40** 332

Makowski A J, Peploswski P and Dembinski S T 2000 *Phys. Lett.* A **266** 241

Manz J 1989 *J. Chem. Phys.* **91** 2190

Meiss J D 1992 *Rev. Mod. Phys.* **64** 795

Nekhoroshev N N 1977 *Russ. Math. Surveys* **32** 1

Oriols X, Martin F and Suné J 1996 *Phys. Rev.* A **54** 2594

Parmenter R H and Valentine R W 1995 *Phys. Lett.* A **201** 1

Parmenter R H and Valentine R W 1997 *Phys. Lett.* A **227** 5

Passon O 2005 *Preprint* quant-ph/0412119v2

Pauli W 1928 *Proc. Solvay Congress* (Paris: Gauthier-Villars)

Pauli W 1953 *Louis de Broglie. Physicien et Penseur* ed G André (Paris: Editions Albin Michel)

Philippidis C, Dewdney C and Hiley B J 1979 *Nuovo Cimento* B **52** 15

Robnik M 1986 *Atomic Spectra and Collisions in External Fielfs* ed K T Taylor, M H Nayhef and C N Clark (New York: Plenum) pp 251–74

Schwengelbeck U and Faisal F H M 1995 *Phys. Lett.* A **199** 281

Sengupta S and Chattaraj P K 1996 *Phys. Lett.* A **215** 119

Skodje R T, Rohrs H W and VanBuskirk J 1989 *Phys. Rev.* A **40** 2894

Valentini A 1991 *Phys. Lett.* A **156** 5

Valentini A and Westman H 2005 *Proc. R. Soc.* A **461** 253

Voglis N, Contopoulos G and Efthymiopoulos C 1998 *Phys. Rev.* E **57** 372

Wisniacki D A, Borondo F and Benito R M 2003 *Europhys. Lett.* **64** 441

Wu H and Sprung D W I 1999 *Phys. Lett.* A **261** 150